Crystallization of Mordenite Platelets using Cooperative Organic Structure-Directing Agents

Manjesh Kumar,[†] Zachariah J. Berkson,[‡] R. John Clark,[†] Yufeng Shen,[†] Nathan A. Prisco,[‡] Qi Zheng,[§] Zhiyuan Zeng,[§,‖] Haimei Zheng,[§,‖] Lynne B. McCusker,[‡,⊥] Jeremy C. Palmer,[†] Bradley F. Chmelka,*[,‡] and Jeffrey D. Rimer*[,†]

[†]Department of Chemical and Biomolecular Engineering, University of Houston, 4726 Calhoun Road, Houston, Texas 77204, United States

[‡]Department of Chemical Engineering, University of California, Santa Barbara, Santa Barbara, California 93106, United States

[§]Materials Sciences Division, Lawrence Berkeley National Laboratory, 1 Cyclotron Road, Berkeley, California 94720, United States

[‖]Department of Materials Science and Engineering, University of California, Berkeley, California 94720, United States

[⊥]Department of Materials, ETH Zurich, Vladimir-Prelog-Weg 5, CH-8093 Zurich, Switzerland

S *Supporting Information*

ABSTRACT: Organic structure-directing agents (OSDAs) are exploited in the crystallization of microporous materials to tailor the physicochemical properties of the resulting zeolite for applications ranging from separations to catalysis. The rational design of these OSDAs often entails the identification of molecules with a geometry that is commensurate with the channels and cages of the target zeolite structure. Syntheses tend to employ only a single OSDA, but there are a few examples where two or more organics operate synergistically to yield a desired product. Using a combination of state-of-the-art characterization techniques and molecular modeling, we show that the coupling of *N,N,N*-trimethyl-1,1-adamantammonium and 1,2-hexanediol, each yielding distinct zeolites when used alone, results in the cooperative direction of a third structure, HOU-4, with the mordenite framework type (**MOR**). Rietveld refinement using synchrotron X-ray diffraction data reveals the spatial arrangement of the organics in the HOU-4 crystals, with amines located in the large channels and alcohols oriented in the side

pockets lining the one-dimensional pores. These results are in excellent agreement with molecular dynamics calculations, which predict similar spatial distributions of organics with an energetically favorable packing density that agrees with experimental measurements of OSDA loading, as well as with solid-state two-dimensional $^{27}Al\{^{29}Si\}$, $^{27}Al\{^1H\}$, and $^{13}C\{^1H\}$ NMR correlation spectra, which establish the proximities and interactions of occluded OSDAs. A combination of high-resolution transmission electron microscopy and atomic force microscopy is used to quantify the size of the HOU-4 crystals, which exhibit a platelike morphology, and to index the crystal facets. Our findings reveal that the combined OSDAs work in tandem to produce ultrathin, nonfaulted HOU-4 crystals that exhibit improved catalytic activity for cumene cracking in comparison to mordenite crystals prepared via conventional syntheses. This novel demonstration of cooperativity highlights the potential possibilities for expanding the use of dual structure-directing agents in zeolite synthesis.

INTRODUCTION

The demand for more efficient zeolite catalysts creates a need to develop new synthesis approaches capable of tailoring crystal properties for optimal performance. Among the many physicochemical properties of zeolites, crystal size plays a significant role in mediating internal mass transport,[1,2] wherein diffusion path lengths of less than 100 nm can markedly improve catalyst lifetime and alter product selectivity.[3] Various approaches have been explored to tune the anisotropic growth of zeolite crystals precisely, including the modification of synthesis conditions, the introduction of growth modifiers,[4] the design of new organic structure-directing agents (OSDAs),[5−9] and the use of crystalline seeds.[10] Achieving materials with well-controlled properties is often challenging, because the

mechanisms of zeolite crystallization[11−14] are complex and poorly understood. Here, we combine state of the art X-ray powder diffraction (XPD) and solid-state NMR character-ization techniques with computer modeling to examine the role of OSDAs in the formation of the mordenite framework type (**MOR**),[15] which is difficult to prepare with submi-crometer dimensions.[16]

Mordenite is a large-pore zeolite (pore diameter ca. 0.7 nm) with unidirectional channels aligned along the *c* axis that is used as a commercial catalyst in reactions such as dehydration of alcohols to olefins,[17] oxidation of methane to methanol,[18]

(hydro)isomerization,[19] cracking,[20] alkylation,[21] and carbonylation.[22] Prior studies have attributed the catalytic activity of mordenite to the intersection of 12-ring channels with 8-ring side pockets (Figure S1) that facilitate shape-selective reactions; however, mordenite is highly susceptible to deactivation owing to mass transport limitations imposed by its one-dimensional pores and large channels that facilitate the formation of polyaromatics (i.e., coke precursors). The reported syntheses of mordenite typically yield large crystallites with sizes that range from 5 to 20 μm and with stacking faults that alter the placement of 8-ring pockets within the channels.[23,24] Postsynthesis modification to introduce mesoporosity is one way of mitigating internal diffusion limitations.[25] Alternatively, the synthesis of crystallites with submicrometer dimensions of the [001] facet can extend the catalyst lifetime. Suib and co-workers have reported sizes as small as 40−60 nm using complicated synthesis protocols that include the use of crystalline seeds,[26] alcohol additives, and/or microwave heating.[27] Mordenite nanorods (ca. 10 × 100 nm) have been synthesized using seeds or cationic gemini surfactants by Xiao[28] and Ryoo[29] and their co-workers, respectively. These syntheses have resulted in nanometer-sized domains within larger aggregates, which similarly involve limitations in internal mass transport.

A combination of inorganic and organic structure-directing agents are often used in zeolite syntheses to regulate the kinetics of crystallization.[30] The synthesis of most zeolites requires the use of OSDA molecules with sizes and shapes that are commensurate with the cages/channels of the target zeolite, thereby facilitating the generation of the desired porous structure.[7] OSDAs are occluded within the framework and are typically removed by postsynthesis calcination. It is common practice to use a single OSDA. In select cases, OSDAs can form clusters (e.g., dimers or aggregates) to stabilize the framework.[31,32] Few syntheses employ two or more different OSDAs. Examples often involve scenarios where only one organic functions as the OSDA and the other alters properties such as crystal size or habit but is a bystander for structure direction.[33] Combinations of OSDAs have also been used to prevent polymorphism in order to improve product purity.[34] Wright and co-workers have demonstrated for zeotypes, such as STA-20, that two organics may be necessary to achieve a desired crystalline phase.[35] In such cases, the OSDAs act cooperatively to produce a product that could not be achieved with either one alone.

Herein, we demonstrate how two OSDAs (one bearing a quaternary amine group and the other an alcohol) cooperatively direct the formation of mordenite crystals with an ultrathin platelet morphology unlike that obtained with conventional methods. The synthesis condition selected for this study produces two different framework types (**MFI**- or **CHA**-type zeolites) when each OSDA is used separately; however, the combination of organics yields mordenite. In order to elucidate the spatial distribution of organics within the channels and side pockets of the mordenite crystals, we used a combination of high-resolution electron microscopy, spectroscopy, and diffraction techniques coupled with molecular modeling to show how the distinct combination of OSDAs works synergistically to direct the mordenite framework structure. A parametric evaluation of synthesis conditions reveals that the judicious selection of OSDAs and growth media and conditions is critical to the formation of mordenite.

■ RESULTS AND DISCUSSION

Our findings have shown that two OSDAs, N,N,N-trimethyl-1,1-adamantammonium (TMAda$^+$) and 1,2-hexanediol (D6$_{1,2}$), work cooperatively to yield a **MOR**-type zeolite, referred to hereafter as HOU-4. TMAda$^+$ is a well-documented OSDA for commercial SSZ-13 (**CHA**) (Figure 1A). The same
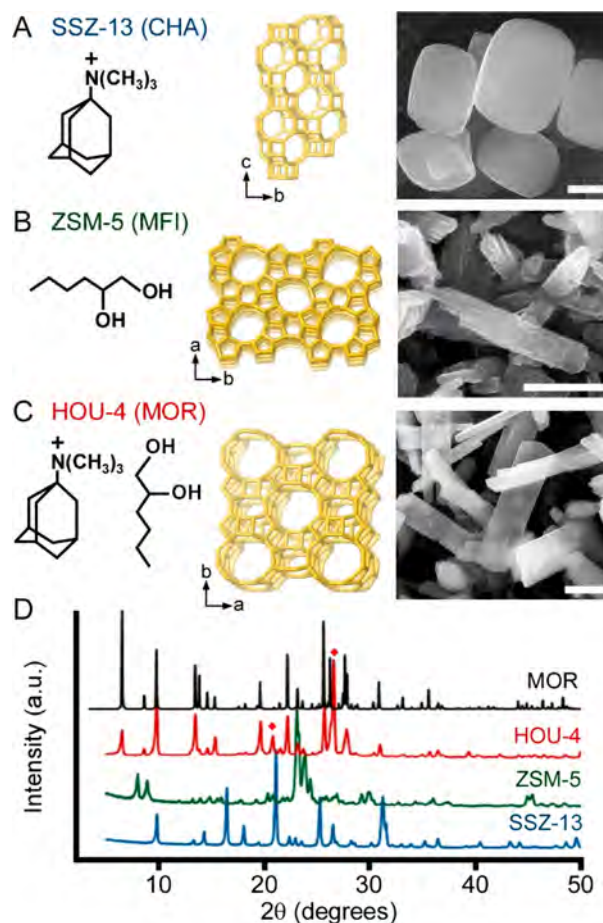

Figure 1. OSDA(s), corresponding zeolite structure, and representative scanning electron micrograph for (A) SSZ-13 (**CHA**) prepared with TMAda$^+$, (B) ZSM-5 (**MFI**) prepared with D6$_{1,2}$ or Na$^+$ ions, and (C) HOU-4 (**MOR**) prepared with TMAda$^+$ and D6$_{1,2}$. Scale bars equal 1 μm. (D) X-ray powder diffraction patterns of the solid precipitates obtained after 6 days of hydrothermal treatment at 180 °C (Table S1) confirming the formation of SSZ-13 (blue), ZSM-5 (green), and HOU-4 (red). The structure of HOU-4 was confirmed using a reference pattern for mordenite (black). Reflections corresponding to a quartz impurity in the HOU-4 sample (Figure S6) are labeled with diamonds. The presence of quartz is attributed to excess silica in the reaction mixture. Parametric studies reduced the quantity of quartz but were unable to eliminate the impurity entirely (see the Supporting Information for more details).

synthesis using only D6$_{1,2}$ results in ZSM-5 (**MFI**) (Figure 1B), whereas an organic-free synthesis with Na$^+$ as an inorganic structure-directing agent also yields ZSM-5 (Figures S2 and S3). Interestingly, the combination of D6$_{1,2}$ and TMAda$^+$ in solutions containing Na$^+$ produces HOU-4 (Figure 1C and Figure S4). Thus, we observe that individual OSDAs and their binary combination generate three different zeolites (Figure 1D): ZSM-5 is a three-dimensional medium-pore zeolite, SSZ-13 is a three-dimensional small-pore zeolite, and mordenite is a one-dimensional large-pore zeolite. The
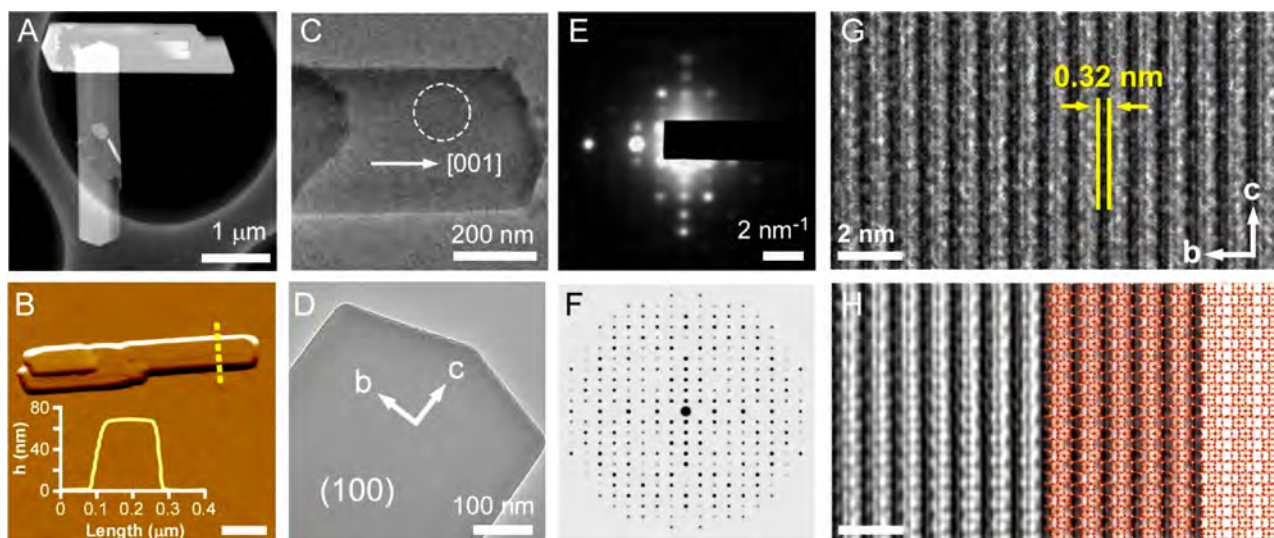
Figure 2. Indexing the habit of HOU-4 crystals. (A) High-angle annular dark-field (HAADF) STEM image of representative HOU-4 crystals taken at low magnification. (B) AFM amplitude mode image of a crystal in air. Inset: height profile measured along the dashed line. The scale bar equals 500 nm. (C) TEM image of a HOU-4 crystal with the [001] growth direction highlighted (arrow). (D) Indexed HOU-4 crystal with a (100) basal surface. (E) Selected area electron diffraction (SAED) pattern of the region in (C) marked by the dashed white circle. The zone axis is [100]. (F) Simulated SAED pattern from [100] based on the mordenite crystal structure (see Figure S12 for patterns of the [010] and [001] zone axes). (G) High-resolution TEM image of a HOU-4 crystal along the [100] zone axis. The black strips could be regarded as pore channels. (H) HRTEM image in (G) after application of a Fourier filter, overlaid with the crystal structure model of mordenite along the [100] direction. Atoms are color-coded as red (oxygen) and yellow (silicon or aluminum).

composite building units (CBUs)[15] of these three structures are different, with the exception of *mor* being shared by both **MFI** and **MOR** framework types (Figure S5). The three zeolites have similar elemental compositions (Table S2) but differ with respect to the crystal habit and quantity of occluded OSDA (Figure S7 and Table S3).

SSZ-13 crystals have a spheroidal morphology with sizes of 1−2 μm and 10 wt % organic (ca. 1.3 TMAda$^+$ per unit cell). ZSM-5 crystals exhibit an indistinct morphology with submicrometer dimensions and contain 5 wt % organic (ca. 2.7 $D6_{1,2}$ per unit cell). HOU-4 crystallizes as thin platelike particles that retain ca. 2 $D6_{1,2}$ and 2 TMAda$^+$ molecules per unit cell, as determined from synchrotron XPD data (Figure S8). All of the $D6_{1,2}$ molecules are removed by postsynthetic washing with water (Figures S9 and S10), which establishes that $D6_{1,2}$ molecules are able to diffuse out of the mordenite nanochannels without appreciable restrictions. The mobility of $D6_{1,2}$ within the large pore channels of mordenite was corroborated by molecular dynamics (MD) simulations (Movie S1). Facile extraction of the diol molecules from zeolite frameworks without the need for postsynthesis calcination is uncommon; therefore, the synthesis of HOU-4 offers a unique route to recover and potentially recycle the OSDAs.

Comparison of transmission electron micrographs from multiple batches (Figure 2A,C,D) show that the width of the HOU-4 crystallites in the [010] direction can reach 1 μm with an average length to width (or [001]/[010]) aspect ratio of 4.0 ± 0.7. Atomic force microscopy (AFM) topographical images of HOU-4 crystals (Figure 2B) reveal an ultrathin habit wherein the analysis of numerous crystals shows a distribution of thicknesses in the [100] direction of around 80 nm (see Figure S11). Selected-area electron diffraction patterns (Figure 2E) were compared against simulated patterns for mordenite along the three principal crystallographic directions (Figure 2F

and Figure S12). These comparisons confirm that the basal surface of HOU-4 is the (100) face. High-resolution TEM (HRTEM, Figure 2G) and the corresponding Fourier filtered image (Figure 2H) show that the 1D channels are oriented parallel to the longest dimension of the HOU-4 crystals. The indexing was further corroborated by overlaying the framework structure of mordenite along the [100] direction on the filtered HRTEM image (Figure 2H), revealing an excellent match. Prior crystallographic analyses of synthetic mordenite commonly assign the six-edged surface as the (001) face.[24,36,37] Indeed, this general morphology is characteristic of most mordenite crystals prepared in the absence of organics (for example, see Figure 6). Assuming that the indexing of the facets of conventional mordenite crystals is correct, it appears that the cooperativity of OSDAs dramatically alters the HOU-4 crystal habit in ways that are neither predictable nor fully understood.

In order to ascertain the spatial arrangement of OSDAs within the zeolite channels, we analyzed an unwashed HOU-4 sample using synchrotron XPD data (Figure 3A) and confirmed that TMAda$^+$ resides within the 12-ring channels (Figure 3B,D), Na$^+$ in the oval 8-ring channels, and $D6_{1,2}$ in the 8-ring side pockets (Figure 3C). Rietveld refinement of the framework structure with occluded structure-directing agents indicates that there are two Na$^+$, two TMAda$^+$, two $D6_{1,2}$ and two water molecules per unit cell. No evidence of crystallite shape anisotropy or stacking faults was apparent in the peak-shape profiles or in the structure refinement. HOU-4 appears to be free of the stacking disorder along the c direction that is present in many mordenite syntheses. Quantitative solid-state one-dimensional (1D) single-pulse ^{13}C and ^{1}H magic-angle-spinning (MAS) NMR analyses (Figure S14) yield a much larger quantity of $D6_{1,2}$ (∼10 $D6_{1,2}$/TMAda$^+$). This suggests that unwashed samples probably retain significant quantities of diol molecules on the particle surfaces, and this is in agreement
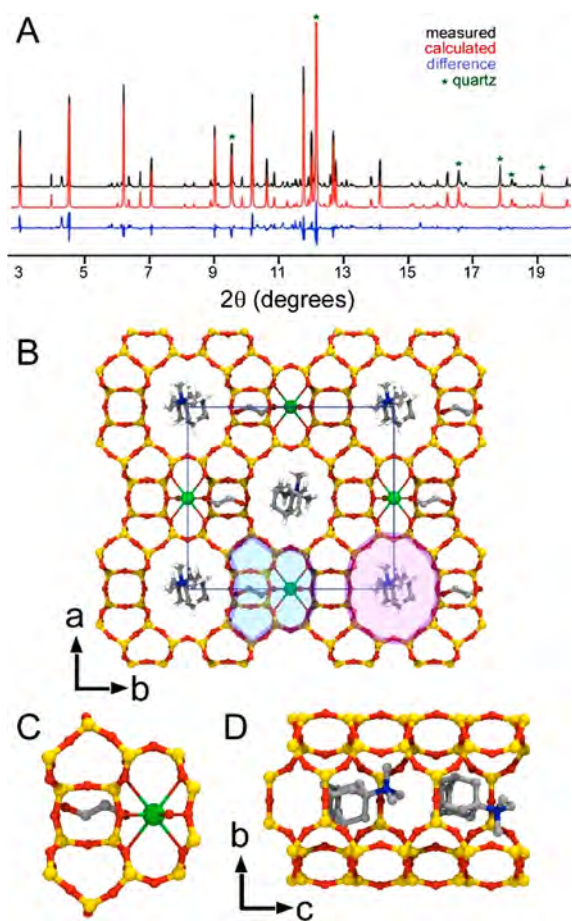
Figure 3. Rietveld refinement of HOU-4 using synchrotron powder diffraction data. (A) Measured (black), calculated (red), and difference profiles (blue) (Table S4). Reflections from a quartz impurity are marked with a green asterisk. (B–D) Arrangement of the nonframework species within the channels of the **MOR** framework compatible with the refined structure of HOU-4 (see also Figure S13): (B) view down the c axis; (C) close-up of the 8-ring side pocket (highlighted in blue in (B)) showing the octahedral coordination of a Na^+ ion to four framework oxygen atoms, one water molecule and one $D6_{1,2}$ molecule; (D) orthogonal view of the 12-ring channel (highlighted in pink in (B)) showing the arrangement of $TMAda^+$ ions along the channel. Atoms are color-coded as gray (carbon), red (oxygen), blue (nitrogen), white (hydrogen), green (sodium), and yellow (T sites occupied by silicon or aluminum).
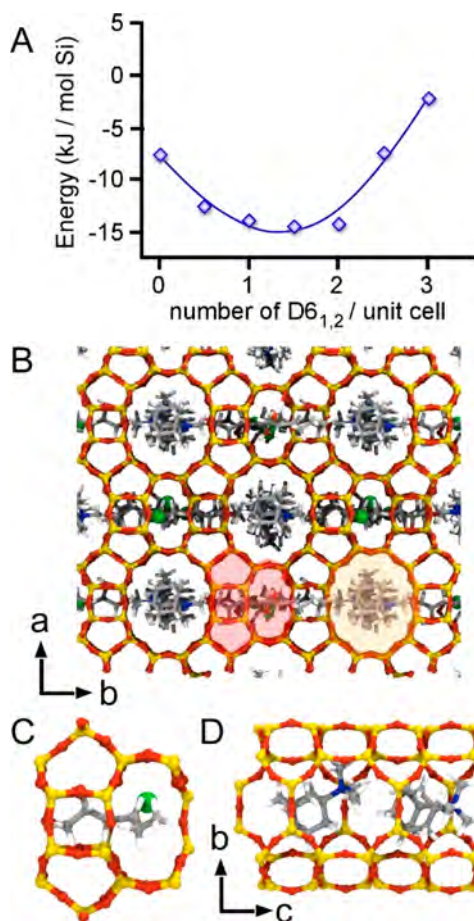

Figure 4. Molecular simulations of organic occlusion in HOU-4 channels. (A) MD calculation of the stabilization energy for organics occluded in mordenite as a function of $D6_{1,2}$ loading using a fixed 1.5 $TMAda^+$ per unit cell. The solid line is a guide for the eye. (B–D) MD simulation of OSDA molecules aligned within the 12-ring channel: (B) view along the c direction; (C) $D6_{1,2}$ aligned within the 8-ring pocket; (D) $TMAda^+$ molecules arranged in the 12-ring channel. Images (C) and (D) contain two Na^+, two $TMAda^+$, and two $D6_{1,2}$ per unit cell. Atoms are color-coded as gray (carbon), red (oxygen), blue (nitrogen), white (hydrogen), green (sodium), and yellow (T sites occupied by silicon or aluminum).

with thermogravimetric analysis of unwashed HOU-4 showing 37 wt% mass loss, consistent with the desorption of surface-adsorbed diol molecules (Figure S7C).

To further understand the role of occluded organics in HOU-4, we performed MD simulations of both OSDAs and Na^+ ions in mordenite. Models placing an increasing amount of alcohol within a single mordenite unit cell at fixed $TMAda^+$ loading (Figure 4A) show that alcohols stabilize the structure, leading to a minimum in the energy profile at around 1.5–2.0 $D6_{1,2}$ molecules per unit cell. This indicates that the alcohol is not merely acting as a space filler[38] but has a significant effect on the energetics of crystallization. As the quantity of $TMAda^+$ per unit cell is increased, less alcohol is required to minimize the energy (Figure S15). In agreement with XPD data revealing the presence of $TMAda^+$ within the large pores of HOU-4, MD simulations show that $TMAda^+$ is energetically favored to be within the 12-ring channels (Figure 4B,D) with

the amine groups oriented in close proximity to the 8-ring pockets. At high $TMAda^+$ loading (two per unit cell), $D6_{1,2}$ molecules are oriented within the 8-ring pockets (Figure 4C), consistent with the XPD refinement. At lower $TMAda^+$ loadings, $D6_{1,2}$ molecules are also observed to reside within the 12-ring channels between adjacent $TMAda^+$ molecules (Figure S16). Hence, both experiment and simulation suggest that the two OSDAs direct the formation of mordenite in a synergistic fashion by stabilizing different features of the framework: $TMAda^+$ directs growth of the 12-ring channels, whereas $D6_{1,2}$ predominantly functions by stabilizing the 8-ring pockets.

The site-specific interactions of different framework [27]Al species with OSDA molecules are established by solid-state two-dimensional (2D) heteronuclear correlation (HETCOR) NMR spectra of HOU-4 (Figure 5). The 2D NMR correlation spectra exploit internuclear dipole–dipole (through-space) or J (through-covalent-bond) couplings and are plotted as 2D contour plots, where correlated signal intensities manifest the mutual proximities or covalent connectivities of the corre-
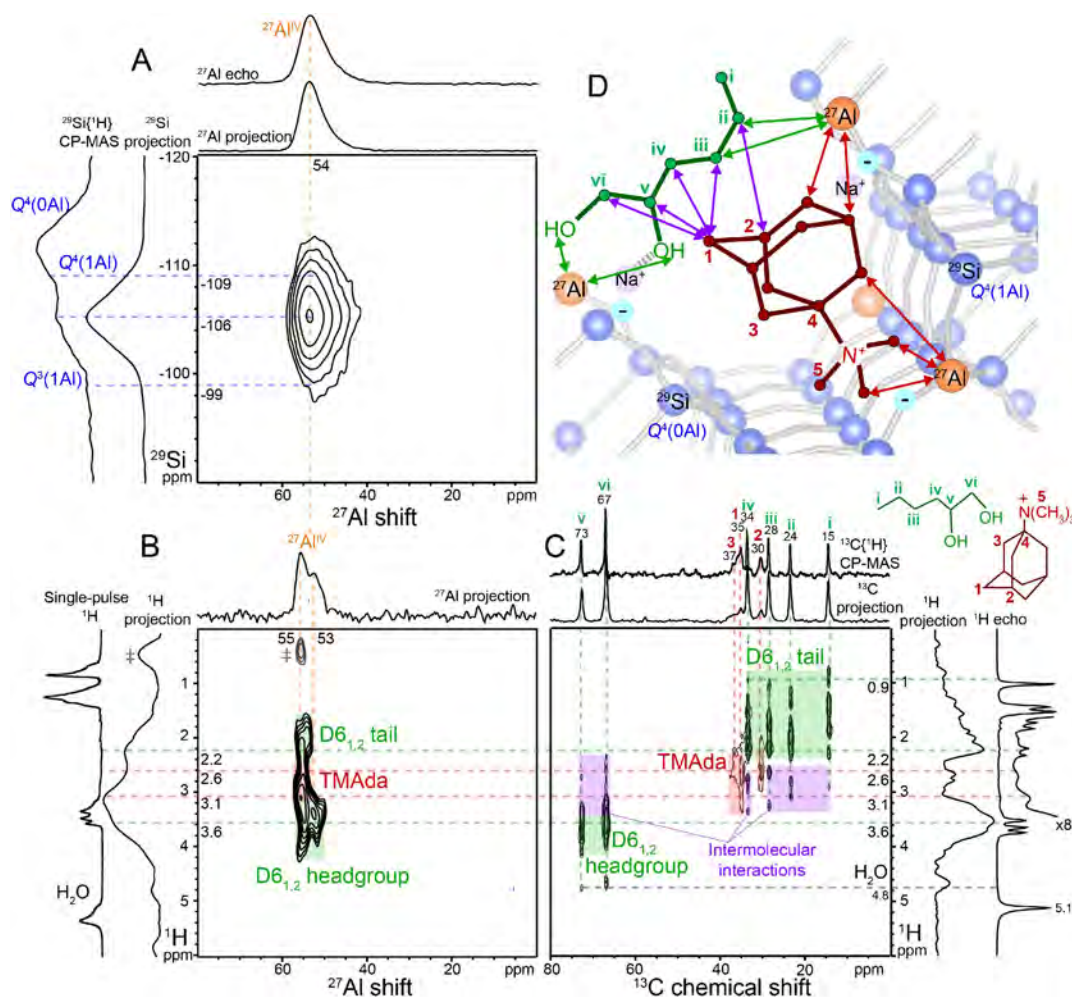
Figure 5. (A) Solid-state 2D ^{27}Al{^{29}Si} J-mediated NMR correlation spectrum acquired at 95 K, 9.4 T, and 10 kHz MAS. (B) Solid-state 2D ^{27}Al{^{1}H} HETCOR spectrum acquired at 263 K, 18.8 T, and 12.5 kHz MAS with a ^{27}Al{^{1}H} contact time of 0.5 ms. The ‡ symbol indicates a center-frequency artifact (for more details refer to the Supporting Information). (C) Solid-state 2D ^{13}C{^{1}H} HETCOR spectrum acquired at 263 K, 11.7 T, and 2.5 kHz MAS with a ^{13}C{^{1}H} contact time of 5 ms. All of the ^{13}C signals are assigned to ^{13}C moieties on the TMAda$^+$ and D6$_{1,2}$ molecules, as indicated in the inset molecular structures. 1D ^{27}Al, ^{13}C{^{1}H}, or ^{1}H MAS NMR spectra acquired under the same conditions are shown along the corresponding ^{27}Al, ^{13}C, or ^{1}H axes for comparison with the 1D projections of the 2D spectra. (D) Schematic diagram of framework-OSDA and intermolecular interactions established by 2D NMR analyses. Green and red arrows indicate framework ^{27}Al interactions with D6$_{1,2}$ and TMAda$^+$ molecules, respectively; purple arrows indicate intermolecular interactions of commingled OSDA molecules.

sponding ^{1}H, ^{13}C, ^{27}Al, or ^{29}Si species.[39,40] For example, covalent ^{27}Al−O−^{29}Si bonds within the HOU-4 frameworks are unambiguously established by the 2D ^{27}Al{^{29}Si} J-mediated NMR correlation spectrum (Figure 5A), which shows a distribution of correlated signal intensity at 54 ppm in the ^{27}Al dimension and −109 to −99 ppm in the ^{29}Si dimension arising from framework aluminum atoms bonded to fully or partially cross-linked ^{29}Si atoms. Previously, such 2D ^{27}Al{^{29}Si} through-bond-mediated correlation spectra of aluminosilicate zeolites have been limited due in part to the low natural isotopic abundance of ^{29}Si (4.7%) and weak ^{27}Al−O−^{29}Si J couplings (<20 Hz) but are enabled here by the improved sensitivity of low-temperature measurement conditions. The ^{27}Al signals exhibit Czjzek lineshapes[41] that reflect a distribution of ^{27}Al heteroatom environments within the mordenite framework and among the four distinct tetrahedral (T) sites, corroborated by complementary ^{27}Al triple-quantum MAS NMR analyses (Figure S17). The relatively small percentage of partially cross-linked ^{29}Si species (ca. 2%, Figure S18) are probably associated with defect sites at the exterior of

the particle surfaces. The Si/Al ratio of HOU-4 estimated by quantitative ^{29}Si MAS NMR is ca. 10 (Figure S18), which is consistent with values of ca. 10 and 13 measured by energy-dispersive X-ray spectroscopy (Table S2) and estimated from synchrotron XPD refinement, respectively.

Different types of framework aluminum sites in as-made HOU-4 are distinguished on the basis of their site-specific interactions with different OSDA molecules, which are established by the 2D ^{27}Al{^{1}H} (Figure 5B) and ^{13}C{^{1}H} HETCOR (Figure 5C) NMR spectra. The HETCOR spectra yield correlated ^{13}C−^{1}H or ^{27}Al−^{1}H signal intensities from ^{13}C−^{1}H or ^{27}Al−^{1}H nuclear spin pairs that are dipole−dipole-coupled through space over subnanometer distances. The different ^{1}H and ^{13}C signals are assigned to ^{1}H and ^{13}C moieties on D6$_{1,2}$ (green shaded regions) or TMAda$^+$ (red shaded regions) molecules by analyses of complementary solid-state 1D and 2D ^{13}C{^{1}H} NMR spectra (Figures S10 and S14) and solution-state 1D ^{13}C NMR spectra of the zeolite synthesis effluent (Figure S19). The 2D ^{27}Al{^{1}H} HETCOR spectrum (Figure 5B) resolves two ^{27}Al signals: one at 55 ppm,

which is correlated to ^1H signals at 2.2 to 3.6 ppm from TMAda$^+$ and D6$_{1,2}$ ^1H moieties, and one at 53 ppm, which is correlated only to the ^1H signal at 3.6 ppm from D6$_{1,2}$ alcohol headgroups coordinated to Na$^+$ cations.[42] These correlated signals evidence two different types of framework ^{27}Al species with either TMAda$^+$ or Na$^+$ cations charge-balancing the associated framework negative charges. As the TMAda$^+$ molecules are sterically hindered from entering the 8-ring mordenite channels, the framework ^{27}Al species proximate to TMAda$^+$ cations are expected to be within the 12-ring channels. Those framework ^{27}Al species associated with charge-balancing Na$^+$ cations are likely located within the 8-ring pockets where the Na$^+$ species are positioned, as determined by the synchrotron XPD analysis (Figure 3) and as corroborated by 2D $^{23}Na\{^1H\}$ HETCOR analyses (Figure S20).

Furthermore, the different OSDA molecules are in close mutual proximities within the mordenite channels, as established by the 2D $^{13}C\{^1H\}$ HETCOR spectrum of HOU-4 (Figure 5C). This spectrum shows correlated signals at 2.2−3.1 ppm in the ^1H dimension and at ^{13}C shifts of 15, 24, 28, 34, 67, and 73 ppm (purple shaded regions) that arise from intermolecular interactions of ^1H environments in TMAda$^+$ molecules and the different ^{13}C environments in proximate (<1 nm) D6$_{1,2}$ molecules. On the basis of complementary 2D $^{29}Si\{^1H\}$ HETCOR spectra (Figure S21) and the synchrotron XPD analyses, we conclude that the different OSDA molecules are intimately commingled within the zeolite pores and act cooperatively (as schematically shown in Figure 5D) during the hydrothermal syntheses of HOU-4 to direct the formation of the mordenite framework and the distribution of Al heteroatoms within both the linear 12-ring channels and the 8-ring pockets.

Parametric studies of HOU-4 synthesis reveal a sensitivity to growth mixture composition (Figures S22−S25). The composition selected for this study (solution C1) falls within the range typically reported for organic-free ZSM-5.[43] Attempts to prepare HOU-4 in growth mixtures more commonly reported for mordenite (i.e., solution C5 with both OSDAs) at higher aluminum content resulted in much larger crystals. Mordenite is typically synthesized using Na$^+$ ions as the sole structure-directing agent, which leads to crystals with a large variance in size and shape (Figure 6). Introduction of D6$_{1,2}$ and/or TMAda$^+$ to conventional synthesis mixtures does not markedly reduce the crystal size. Indeed, the growth mixture that generates HOU-4 is adopted from a SSZ-13 synthesis,[44] where we have reported D6$_{1,2}$ to be an effective modifier of SSZ-13 crystallization at low concentration (i.e., molar ratios less than 1.0 D6$_{1,2}$ to 1.0 SiO$_2$). Under such conditions, the diol reduces the size of SSZ-13 crystals by 1 order of magnitude; however, increased diol content (i.e., molar ratios in excess of 1.6 D6$_{1,2}$ to 1.0 SiO$_2$) shifts its role from that of crystal growth modifier to an OSDA that operates synergistically with TMAda$^+$ to direct the formation of ultrathin mordenite crystals. This reveals that HOU-4 requires a threshold amount of diol and growth mixtures with much higher silicon content than are typically required for conventional mordenite synthesis.

The formation of HOU-4 and its purity are sensitive to the carbon length of the diol. For example, combinations of TMAda$^+$ with either 1,2-pentanediol (Figure 7A) or 1,2-butanediol (Figure S25) lead to a SSZ-13 impurity, whereas 1,2-propanediol (Figure 7B) results in pure SSZ-13. Diols with
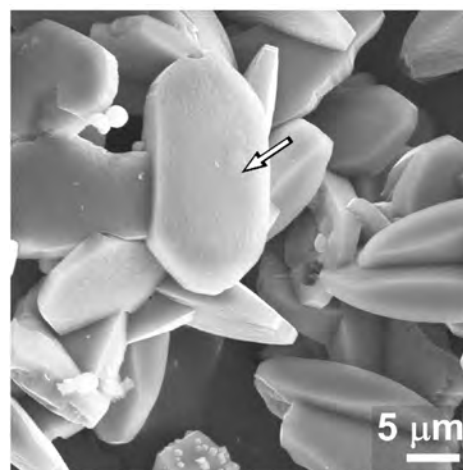

Figure 6. Scanning electron micrograph of a conventional mordenite prepared by an organic-free synthesis using Na$^+$ as an inorganic structure-directing agent. The arrow highlights a six-edged surface that is characteristic of many **MOR**-type crystals reported in the literature. This surface is commonly indexed as the (001) face.
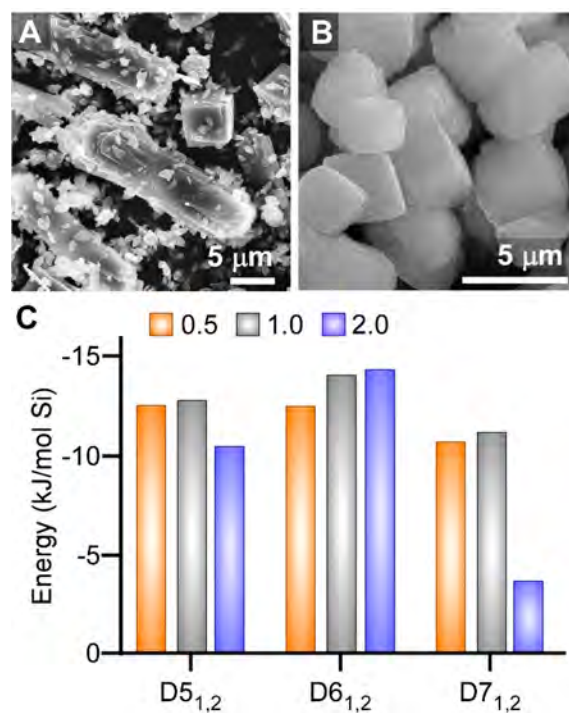

Figure 7. Scanning electron micrographs of the HOU-4 synthesis using a combination of TMAda$^+$ with (A) 1,2-pentanediol and (B) 1,2-propanediol. Crystals in (A) contain mixed phases of mordenite and SSZ-13 (isometric crystals), while those in (B) are pure SSZ-13 by XPD. (C) Stabilization energy from MD calculations as a function of x alcohols per unit cell (x = 0.5, 1.0, 2.0) for a fixed loading of 1.5 TMAda$^+$ per unit cell. We find that D6$_{1,2}$ at a loading of 1.0−2.0 molecules per unit cell provides the greatest stabilization.

carbon lengths in excess of six were not tested owing to their immiscibility in water. The results of diol substitution are consistent with MD simulations of mordenite with TMAda$^+$ and diols of varying carbon length. At a fixed TMAda$^+$ content and varying diol quantities, the minimum in the stabilization energy (Figure 7C) for D6$_{1,2}$ indicates that the combination of this diol with TMAda$^+$ is an energetically favorable pairing for

HOU-4 synthesis, consistent with experimental observations. Thus, both experiment and simulation suggest that $D6_{1,2}$ is optimal in size to span the 8-ring pockets and direct their growth.

It is not fully understood how the platelike morphology of HOU-4 crystals is derived from the combined structure-directing influences of TMAda$^+$ and $D6_{1,2}$ molecules. The dual action of organics enhances growth along the direction of channels (*c* direction) while hindering growth in the *a* direction. The role of cooperative OSDAs in HOU-4 crystallization is seemingly unrelated to that of a growth modifier which alters the crystal morphology in conventional mordenite synthesis, as neither organic solely produces thin crystals. In fact, the presence of $D6_{1,2}$ has the opposite effect in conventional mordenite syntheses, where it increases crystal thickness in the absence of TMAda$^+$ (Figure S26) relative to the control (Figure 6). The ability to prepare nanosized crystals has significant implications for catalytic applications. Zeolite catalysts with restricted mass transport, such as mordenite and other one-dimensional framework types, are the most susceptible to rapid deactivation by coking. Comparisons between HOU-4 and conventional mordenite crystals reveal that the crystal dimensions along the *c* direction (parallel to the large-pore channels) are comparable, on the order of a micrometer; however, the generation of ultrathin platelets leads to higher specific surface area, which can influence catalytic performance. To illustrate this point, we prepared acid forms of the platelets (H-HOU-4) and conventional crystals (H-mordenite). For catalytic testing we selected a reaction where shape selectivity was not critical in order to assess differences in catalyst activity. To this end, we used cumene cracking as a model reaction to evaluate time-on-stream lifetime. The total number of acid sites on each sample was quantified by NH$_3$ temperature-programmed desorption (TPD). Tests in a packed-bed reactor at 450 °C reveal that the turnover number (evaluated in the shaded regions of Figure 8) is much larger for H-HOU-4 (38.7 mol cumene/mol H$^+$) in comparison to conventional mordenite (10.3 mol cumene/mol H$^+$) owing to the faster rate of H-mordenite deactivation. These results are qualitatively consistent with studies of nanosized zeolite catalysts in the literature[2,45] that generally report much longer lifetimes owing to reduced mass transport limitations. For the study reported here, external acid sites probably play a role in the observed differences; however, it remains to be determined if the lack of stacking faults in HOU-4 improves internal mass transport and contributes to its improved lifetime. The different synthesis conditions may also yield distinct distributions of framework Al heteroatoms and associated Brønsted acid sites in H-mordenite and H-HOU-4, which would influence the catalytic activity and stability. Rationalizing the differences in catalyst performance is a topic of ongoing investigation.

■ CONCLUSION

The generation of HOU-4 crystallites using a combination of two organics is one of only a few reported cases where multiple OSDAs work cooperatively to direct zeolite crystallization and structure. Using a collection of high-resolution characterization and modeling techniques, we are able to resolve the locations of both OSDAs in the pores of HOU-4. Combined synchrotron XPD, 2D solid-state NMR, HRTEM, and molecular modeling analyses reveal the framework structure and local compositions, types of framework−organic inter-
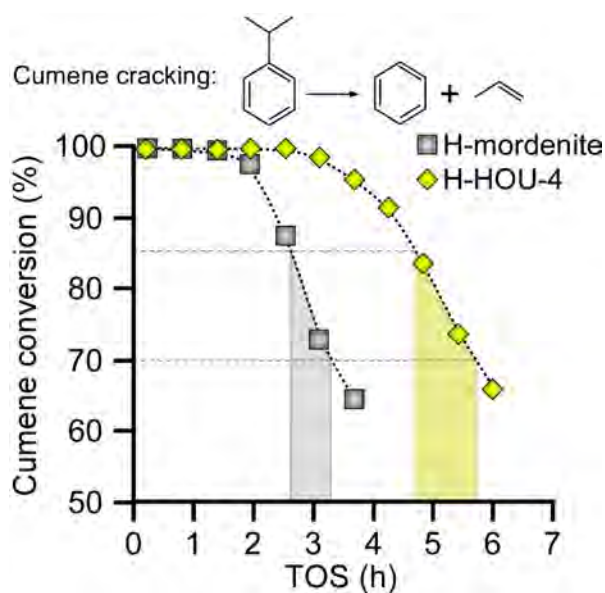

Figure 8. Comparative catalytic performance of H-mordenite crystals (Si/Al = 8 by EDX) from a conventional synthesis and H-HOU-4 crystals (Si/Al = 9.5 by EDX). Cumene cracking was performed in a packed-bed reactor at 450 °C using a weight hourly space velocity (WHSV) of 2 h^{-1}. The shaded regions were used to calculate catalyst turnover number using the density of acid sites as determined by NH$_3$-TPD to account for the different number of active (Brønsted acid) sites for each catalyst.

actions, and relative distributions of organics within the 12-ring channels and 8-ring pockets of mordenite. The combination of these complementary techniques offers unparalleled insight into the roles of different OSDAs in directing zeolite crystallization to achieve distinct properties. We expect that the methods and analyses reported here can be extended to ascertain how SDAs tailor zeolite crystal size, shape, and composition. Indeed, one challenge in zeolite synthesis is determining how multiple organic and inorganic structure-directing species function in a concerted manner to influence the physicochemical properties of zeolites and control crystal polymorphism a priori. A unique aspect of HOU-4 crystallization is the role of nonionic alcohols, which interact relatively weakly with crystallizing zeolite frameworks and are rarely employed as OSDAs in zeolite syntheses. Here, diol molecules work in tandem with cationic Na$^+$ and TMAda$^+$ species to stabilize the different linear nanopore networks in mordenite.

The synthesis of nonfaulted submicrometer mordenite crystals has been a significant challenge. In this study, we have shown that the ability to prepare mordenite crystals with reduced stacking faults and high surface area improves the catalyst lifetime 4-fold relative to materials prepared by conventional methods. Collectively, our findings suggest that further exploration into the use of cooperative organics in zeolite syntheses holds considerable promise for the engineering and optimization of microporous materials.

■ EXPERIMENTAL SECTION

Materials. The following chemicals were used as reagents: Cab-O-Sil (M-5, Spectrum Chemical), silica gel (91%, Sigma-Aldrich), sodium hydroxide (98% pellets, MACRON Fine Chemicals), *N,N,N*-trimethyl-1,1-adamantammonium hydroxide (TMAda-OH, 25 wt % in water, SACHEM Inc.), 1,2-hexanediol ($D6_{1,2}$, 98%), 1,2-

pentanediol (D5$_{1,2}$, 96% Aldrich), 1,2-butanediol (D4$_{1,2}$, ≥98%, Sigma-Aldrich), 1,2-propanediol (D3$_{1,2}$, ≥99.5%, Sigma-Aldrich), and aluminum hydroxide (80.3 wt % Al(OH)$_3$, SPI0250 hydrogel). It should be noted that the IUPAC names for the two OSDAs used in this study are hexane-1,2-diol and 1-adamantyl(trimethyl)azanium. Ion exchange was performed using ammonium nitrate (ACS reagent ≥98%, Sigma-Aldrich). Deionized (DI) water used in all experiments was purified with an Aqua Solutions RODI-C-12A purification system (18.2 MΩ). All reagents were used as received without further purification.

Synthesis of Mordenite. Mordenite (HOU-4) was synthesized with the OSDA N,N,N-trimethyl-1,1-adamantammonium hydroxide (TMAda-OH) and 1,2-hexanediol (D6$_{1,2}$) using solutions with a molar composition of 0.052 Al(OH)$_3$/1.0 SiO$_2$/0.2 NaOH/44 H$_2$O/0.1 TMAda-OH/1.6 1,2-hexanediol. Sodium hydroxide (0.09 g, 0.0022 mol) was first dissolved in water (8.21 g, 0.4959 mol), followed by the addition of TMAda-OH (0.95 g, 0.0011 mol) and 1,2-hexanediol (2.17 g, 0.018 mol). This solution was stirred until it was clear (ca. 15 min). Aluminum hydroxide (0.06 g, 0.0005 mol) was added to the solution, and this mixture was stirred for another 15 min at room temperature. To this clear solution was added the silica source (0.67 g, 0.0112 mol), and the resulting mixture was first manually stirred with a plastic rod for ca. 15 min, followed by continuous stirring using a stir bar (400 rpm) for 4 h at 80 °C in a mineral oil bath. Approximately 10 g of growth solution after 4 h of heated stirring was placed in a Teflon-lined stainless steel acid digestion bomb (Parr Instruments) and was heated under rotation (~30 rpm) and autogenous pressure in a Thermo-Fisher Precision Premium 3050 Series gravity oven. The nominal time and temperature for HOU-4 synthesis was 6 days at 180 °C. The products of all syntheses were isolated as a white powder (ca. 600 mg) by centrifuging the mother liquor (13000 rpm for 45 min) for three cycles with DI water washes. Samples for microscopy were prepared by first redispersing a small amount of powder (ca. 5 mg) in DI water. An aliquot of this solution was placed on a glass slide and dried overnight. Crystals were transferred to metal sample disks for microscopy studies by contacting the glass slide with carbon tape for SEM.

Conventional mordenite was synthesized using a growth solution with a molar composition of 1 Al$_2$O$_3$/30 SiO$_2$/5 Na$_2$O/780 H$_2$O.[26,46] Sodium hydroxide (0.25 g, 0.0061 mol) was first dissolved in water (8.437 g, 0.468 mol), followed by the addition of sodium aluminate (0.1003 g, 0.00061 mol). The solution was stirred until it was clear (ca. 15 min), followed by the addition of silica gel (1.212 g, 0.0183 mol), and the resulting mixture was stirred at 400 rpm for 4 h. Approximately 10 g of the growth mixture was placed in a Teflon-lined stainless steel acid digestion bomb and was heated under static and autogenous pressure. The nominal time and temperature for synthesis was 4 days and 170 °C, respectively. The products of all syntheses were isolated from mother liquor using vacuum filtration and a 0.45 μm membrane filter with copious amounts of DI water washes. Samples for microscopy were prepared as described above.

Solid-State Nuclear Magnetic Resonance (NMR). Solid-state 1D and 2D ^{1}H, ^{13}C, ^{27}Al, and ^{29}Si MAS NMR spectroscopy was used to analyze the ^{1}H, ^{13}C, ^{27}Al, and ^{29}Si environments in as-made HOU-4 crystallites. The 2D ^{27}Al{^{29}Si} J-mediated NMR correlation spectrum (Figure 3A) was acquired on a Bruker ASCEND 400 MHz (9.4 T) DNP NMR spectrometer operating at Larmor frequencies of 400.203, 104.283, and 79.501 MHz for ^{1}H, ^{27}Al, and ^{29}Si nuclei, respectively. This instrument is equipped with a 3.2 mm triple-resonance HXY low-temperature MAS probehead. Low-temperature measurement conditions of 95 K were used for improved signal sensitivity. The spectrum was acquired using a 2D heteronuclear multiple quantum correlation (HMQC) pulse sequence[47,48] with an experimentally optimized half-echo τ delay of 20 ms used to refocus the weak (ca. 1/(4τ) = 12.5 Hz) through-bond ^{27}Al–O–^{29}Si J couplings. The signal sensitivity was enhanced by applying a 1 ms ^{27}Al adiabatic double-frequency sweep pulse during the preparation period to invert the ^{27}Al satellite transitions.[49] During the rotor-synchronized τ delay periods, 100 kHz of continuous wave ^{1}H decoupling was

applied. A recycle delay time of 1 s was used with a rotor-synchronized t_1 increment step size of 100 μs, 96 t_1 increments, and 256 transients for a total acquisition time of 7 h. The 2D ^{29}Si{^{1}H} and ^{13}C{^{1}H} spectra were acquired on a Bruker AVANCE 500 MHz (11.7 T) wide-bore spectrometer operating at Larmor frequencies of 500.222, 125.789, and 99.369 MHz for ^{1}H, ^{13}C, and ^{29}Si, respectively. Recycle delay times of 0.75 s were used with t_1 increment step sizes of 128 μs. The 2D ^{29}Si{^{1}H} HETCOR spectrum acquired at a short contact time (0.5 ms, Figure 3B) was acquired with 196 t_1 increments and 256 transients for a total acquisition time of 10.5 h. The 2D ^{29}Si{^{1}H} HETCOR spectrum acquired at a longer contact time (5 ms, Figure S19) was acquired with 256 t_1 increments and 64 transients for a total acquisition time of 3.5 h. The 2D ^{13}C{^{1}H} HETCOR spectra acquired with contact times of 0.5 and 5 ms (Figure S10) were acquired respectively with 250 and 430 t_1 increments and 512 and 128 transients for total acquisition times of 27 and 11.5 h. The 2D ^{27}Al{^{1}H} (Figure 3C) and ^{23}Na{^{1}H} (Figure S20) HETCOR spectra were acquired on a Bruker AVANCE-III Ultrashield Plus 800 MHz (18.8 T) narrow-bore spectrometer operating at Larmor frequencies of 208.527, 211.681, and 800.242 MHz for ^{27}Al, ^{23}Na, and ^{1}H, respectively, and a Bruker 3.2 mm broad-band double-resonance HX probehead was used. The 2D ^{27}Al{^{1}H} HETCOR spectrum was acquired with a repetition time of 1 s, 50 t_1 increments, and 512 transients for a total acquisition time of 7 h. The 2D ^{23}Na{^{1}H} HETCOR spectrum was acquired with a repetition time of 1 s, 32 t_1 increments, and 1024 transients for a total acquisition time of 9 h. All of the 2D HETCOR spectra were acquired using homonuclear ^{1}H–^{1}H eDUMBO-1$_{22}$ decoupling[50] during the ^{1}H evolution periods to improve resolution in the ^{1}H dimensions. For the 2D ^{29}Si{^{1}H}, ^{13}C{^{1}H}, ^{23}Na{^{1}H}, and ^{27}Al{^{1}H} HETCOR experiments, a variable-temperature chiller unit was to lower the sample temperature to approximately 263 K to reduce the mobility of the OSDA species and improve cross-polarization signal sensitivity. All of the 1D and 2D spectra were acquired with 100 kHz heteronuclear SPINAL-64[51] ^{1}H decoupling during the acquisition period.

Atomic Force Microscopy (AFM). AFM measurements were performed in air using an Asylum Research MFP-3D-SA instrument (Santa Barbara, CA). An aliquot of HOU-4 dispersed in water was placed on a silicon wafer and was allowed to dry at room temperature. The silicon wafer was calcined at 500 °C for 5 h, followed by cleaning under an inert Ar gas flow to remove loosely bound crystals. AFM images were collected using a Cr/Au-coated silicon nitride cantilever (Olympus RC800PB with a spring constant of 0.82 N/m) in contact mode at a scan rate of 1.2 Hz and 256 lines/scan.

Electron Microscopy. Scanning electron microscopy (SEM) was performed with a FEI 235 dual-beam (focused ion beam) system operated at 15 kV and a 5 mm working distance. All SEM samples were coated with a thin carbon layer (ca. 20 nm) prior to imaging. Transmission electron microscopy (TEM) was carried out for structural and morphology characterization using a Thermo Fischer (formerly FEI) 200 kV TitanX transmission electron microscope equipped with a windowless SDD Bruker EDS detector with fast processor.

X-ray Analysis. Energy-dispersive X-ray spectroscopy (EDX) was performed using a JEOL JSM 6330F field emission SEM at a working distance of 15 mm and voltage of 15 kV and 12 mA. X-ray powder diffraction (XPD) patterns of as-made zeolite samples were collected on a Siemens D5000 X-ray diffractometer using a Cu Kα_1 source (40 kV, 30 mA). For reference intensity ratio (RIR) analysis using mordenite–quartz mixtures, a Rigaku SmartLab diffractometer (40 kV, 44 mA) was used. The **MOR**-type framework was confirmed using a reference pattern from the Database of Zeolite Structures.[15] Synchrotron powder diffraction data were collected on an unwashed sample of HOU-4 in a 0.5 mm glass capillary on the Materials Science Beamline at the Swiss Light Source (SLS) in Villigen, Switzerland.[52] The wavelength was determined from a Si standard to be 0.7087 Å. Additional details of XPD analysis are provided in the Supporting Information.

Molecular Dynamics (MD) Simulations. MD simulations were performed with GROMACS 4.6.7.[53] The MOR zeolite framework was modeled as an all-silica structure using the ClayFF potential,[54] whereas the OSDAs (TMAda$^+$, 1,2-pentanediol, 1,2-butanediol, 1,2-hexanediol, and 1,2-heptanediol) were described using the generalized AMBER force field.[55] Atomic positions and lattice parameters for the mordenite framework were taken from the Database of Zeolite Structures. Na$^+$ ions were inserted into the 8-ring pockets, in the positions suggested by XRPD analysis (Figure S13). Although Na$^+$ ions stabilize Al in the framework, the positions of the Al sites are not precisely known. Consequently, Al was implicitly modeled by smearing a negative charge over the oxygens in the 8-ring pockets to counterbalance the Na$^+$ ions and ensure electroneutrality. Potential parameters for describing van der Waals interactions between the OSDAs and zeolite framework atoms were evaluated using standard Lorentz–Berthelot combining rules.[56] van der Waals and real-space Coulombic interactions were truncated using a cutoff of 0.9 nm, and the particle mesh Ewald method[56] was used to treat long-range electrostatics, with parameters chosen to ensure a relative error of less than 10^{-4} in the calculated energy. The equations of motion were propagated using a leapfrog integration scheme with a 2 fs time step.[56] The temperature and pressure of the system were maintained using a Bussi–Parrinello velocity-rescaling thermostat[57] and a Parrinello–Rahman barostat,[58] respectively. The relaxation time constants for both the thermostat and barostat were set to 2 ps.

Following our recent study of surfactant occlusion in MFI structured zeolites,[59] energetically favorable conformations for the OSDAs in mordenite were sampled using a three-step procedure. First, the OSDAs were gradually inserted into the zeolite framework using the alchemical transformation procedure described by Kim et al.,[60] whereby the OSDAs were converted from an ideal gas to fully interacting molecules over the course of a short MD simulation (500 ps) at ambient temperature. This gradual insertion step ensured that the system did not become trapped in unphysical, high-energy conformations. Next, the conjugate gradient algorithm was used to minimize the configurational energy of the system. Finally, the configuration from the energy minimization step was use to initialize a nanosecond-long MD simulation at 300 K and 0 bar. Data from the last half of the MD trajectory were used to evaluate the stabilization energy[61,62] $E_s \equiv \langle U_{sys} \rangle - \langle U_{zeo} \rangle - \sum_i n_i \langle U_{SDA,i} \rangle$, where $\langle U_{sys} \rangle$ is the average energy of the system, $\langle U_{zeo} \rangle$ is the average energy of the empty zeolite framework, n_i is the number of inserted OSDA molecules of type i, and $\langle U_{SDA,i} \rangle$ is the average energy computed for a single OSDA molecule under vacuum. The steps above were repeated to evaluate E_s for $\sim 10^3$ different conformations at each OSDA loading considered in the study. Conformations with low E_s values (lowest 10%) were saved for subsequent analysis.

Catalyst Preparation and Testing. Samples for catalysis were calcined in a Thermo Fisher Lindberg Blue furnace under a constant flow of 100 sccm dried air (Matheson Tri-Gas) at 550 °C for 5 h with a temperature ramping/cooling rate of 1 °C/min. These samples were converted to an acid form (Brønsted acids) by ion exchange, wherein the calcined zeolite was mixed with 1.0 M ammonium nitrate solution to obtain a 2 wt % suspension. This mixture was heated to 80 °C for 2 h to allow the exchange of Na$^+$ with NH$_4^+$. This process was performed three times with centrifugation/washing between each ion exchange cycle. The final NH$_4$–eolite samples were washed three times with DI water before they were calcined once again under the same conditions stated above, thus becoming H-form zeolite.

Cumene cracking over H-form catalysts was carried out in a 1/4 in. stainless steel tube installed in a Thermo Scientific Lindberg Blue M furnace. The catalyst bed was supported between two plugs of quartz wool, and a K-type thermocouple (Omega Engineering) was inserted into the stainless tube to measure the temperature of the catalyst bed. Prior to the reaction, the catalyst bed was pretreated in situ at 550 °C for 3 h under a flow of dried air (6 cm^3/min of O$_2$, 24 cm^3/min of N$_2$). After this pretreatment, the catalyst bed was cooled to the reaction temperature: i.e. 450 °C. Cumene (98%, Sigma-Aldrich) was fed by a syringe pump (Harvard Apparatus) at 2 μL/min into a

heated inert gas stream of Ar (50 cm^3/min), which resulted in a reactant flow with a weight hourly space velocity (WHSV) of 2 h^{-1}. The cumene conversion is defined as the percentage of cumene reacted at the effluent of the catalyst bed. To compare the deactivation rate between different catalyst samples, the turnover number (TON) is calculated for a selected span of time-on-stream (TOS) using a modified form of the equation reported by Bhan and co-workers[63]

$$\mathrm{TON}(t) = \frac{1}{[\mathrm{H}^+]_0} \int_{t_1}^{t_2} F(\tau)\, \mathrm{d}\tau \tag{1}$$

where $[\mathrm{H}^+]_0$ is the total number of Brønsted acid sites (obtained from the NH$_3$-TPD data in Table S3), $F(\tau)$ is the molar flow rate of converted carbon (reacted cumene), and t is the TOS selected between times t_1 and t_2 corresponding to 85 and 70% cumene conversion, respectively (i.e., regions of nearly linear deactivation in Figure 8).

Temperature-Programmed Desorption of Ammonia (NH$_3$-TPD). Temperature-programmed desorption of ammonia was performed by the Bhan group (University of Minnesota) on a Micromeritics Autochem II 2920 equipped with a TCD detector. Prior to TPD, ca. 100 mg of catalyst was first outgassed in He for 1 h at 600 °C with a heating ramp of 10 °C min^{-1}. Ammonia was adsorbed at 100 °C until saturatation, followed by flushing with He for 120 min at 100 °C. The ammonia desorption was monitored using a TCD detector until an upper temperature of 600 °C was reached with a ramp of 10 °C min^{-1}, using a flow of 25 mL min^{-1}.

■ ASSOCIATED CONTENT

ⓢ Supporting Information

The Supporting Information is available free of charge at https://pubs.acs.org/doi/10.1021/jacs.9b09697.

> Additional details of materials characterization, including XRD patterns, SEM and TEM images, TGA profiles, elemental analysis, solid-state NMR, AFM images and height profiles, details of molecular modeling, and examples of alternative synthesis conditions employing variants of OSDAs and the addition of modifiers (PDF)
> Molecular dynamics simulations (MP4)

■ AUTHOR INFORMATION

Corresponding Authors
*E-mail for B.F.C.: bradc@engineering.ucsb.edu.
*E-mail for J.D.R.: jrimer@central.uh.edu.

ORCID ⊙
Zachariah J. Berkson: 0000-0002-2157-4172
Yufeng Shen: 0000-0001-9777-4691
Zhiyuan Zeng: 0000-0001-7483-1438
Haimei Zheng: 0000-0003-3813-4170
Jeremy C. Palmer: 0000-0003-0856-4743
Bradley F. Chmelka: 0000-0002-4450-6949
Jeffrey D. Rimer: 0000-0002-2296-3428

Author Contributions
All authors have given approval to the final version of the manuscript.

Notes
The authors declare no competing financial interest.

■ ACKNOWLEDGMENTS

■ REFERENCES

(1) Ng, E. P.; Chateigner, D.; Bein, T.; Valtchev, V.; Mintova, S. Capturing Ultrasmall EMT Zeolite from Template-Free Systems. *Science* **2012**, *335* (6064), 70−73.

(2) Zhang, X. Y.; Liu, D. X.; Xu, D. D.; Asahina, S.; Cychosz, K. A.; Agrawal, K. V.; Al Wahedi, Y.; Bhan, A.; Al Hashimi, S.; Terasaki, O.; Thommes, M.; Tsapatsis, M. Synthesis of Self-Pillared Zeolite Nanosheets by Repetitive Branching. *Science* **2012**, *336* (6089), 1684−1687.

(3) Olsbye, U.; Svelle, S.; Bjorgen, M.; Beato, P.; Janssens, T. V. W.; Joensen, F.; Bordiga, S.; Lillerud, K. P. Conversion of Methanol to Hydrocarbons: How Zeolite Cavity and Pore Size Controls Product Selectivity. *Angew. Chem., Int. Ed.* **2012**, *51* (24), 5810−5831.

(4) Rimer, J. D.; Kumar, M.; Li, R.; Lupulescu, A. I.; Oleksiak, M. D. Tailoring the physicochemical properties of zeolite catalysts. *Catal. Sci. Technol.* **2014**, *4* (11), 3762−3771.

(5) Bereciartua, P. J.; Cantin, A.; Corma, A.; Jorda, J. L.; Palomino, M.; Rey, F.; Valencia, S.; Corcoran, E. W.; Kortunov, P.; Ravikovitch, P. I.; Burton, A.; Yoon, C.; Wang, Y.; Paur, C.; Guzman, J.; Bishop, A. R.; Casty, G. L. Control of zeolite framework flexibility and pore topology for separation of ethane and ethylene. *Science* **2017**, *358* (6366), 1068−1071.

(6) Brand, S. K.; Schmidt, J. E.; Deem, M. W.; Daeyaert, F.; Ma, Y. H.; Terasaki, O.; Orazov, M.; Davis, M. E. Enantiomerically enriched, polycrystalline molecular sieves. *Proc. Natl. Acad. Sci. U. S. A.* **2017**, *114* (20), 5101−5106.

(7) Gallego, E. M.; Portilla, M. T.; Paris, C.; León-Escamilla, A.; Boronat, M.; Moliner, M.; Corma, A. Ab initio" synthesis of zeolites for preestablished catalytic reactions. *Science* **2017**, *355* (6329), 1051.

(8) Na, K.; Jo, C.; Kim, J.; Cho, K.; Jung, J.; Seo, Y.; Messinger, R. J.; Chmelka, B. F.; Ryoo, R. Directing Zeolite Structures into Hierarchically Nanoporous Architectures. *Science* **2011**, *333* (6040), 328−332.

(9) Simancas, R.; Dari, D.; Velamazan, N.; Navarro, M. T.; Cantin, A.; Jorda, J. L.; Sastre, G.; Corma, A.; Rey, F. Modular Organic Structure-Directing Agents for the Synthesis of Zeolites. *Science* **2010**, *330* (6008), 1219−1222.

(10) Jeon, M. Y.; Kim, D.; Kumar, P.; Lee, P. S.; Rangnekar, N.; Bai, P.; Shete, M.; Elyassi, B.; Lee, H. S.; Narasimharao, K.; Basahel, S. N.; Al-Thabaiti, S.; Xu, W. Q.; Cho, H. J.; Fetisov, E. O.; Thyagarajan, R.; DeJaco, R. F.; Fan, W.; Mkhoyan, K. A.; Siepmann, J. I.; Tsapatsis, M. Ultra-selective high-flux membranes from directly synthesized zeolite nanosheets. *Nature* **2017**, *543* (7647), 690−694.

(11) De Yoreo, J. J.; Gilbert, P.; Sommerdijk, N.; Penn, R. L.; Whitelam, S.; Joester, D.; Zhang, H. Z.; Rimer, J. D.; Navrotsky, A.; Banfield, J. F.; Wallace, A. F.; Michel, F. M.; Meldrum, F. C.; Colfen, H.; Dove, P. M. Crystallization by particle attachment in synthetic, biogenic, and geologic environments. *Science* **2015**, *349* (6247), aaa6760.

(12) Morris, S. A.; Bignami, G. P. M.; Tian, Y.; Navarro, M.; Firth, D. S.; Cejka, J.; Wheatley, P. S.; Dawson, D. M.; Slawinski, W. A.; Wragg, D. S.; Morris, R. E.; Ashbrook, S. E. In situ solid-state NMR and XRD studies of the ADOR process and the unusual structure of zeolite IPC-6. *Nat. Chem.* **2017**, *9* (10), 1012−1018.

(13) Olafson, K. N.; Li, R.; Alamani, B. G.; Rimer, J. D. Engineering Crystal Modifiers: Bridging Classical and Nonclassical Crystallization. *Chem. Mater.* **2016**, *28* (23), 8453−8465.

(14) Berkson, Z. J.; Messinger, R. J.; Na, K.; Seo, Y.; Ryoo, R.; Chmelka, B. F. Non-Topotactic Transformation of Silicate Nanolayers into Mesostructured MFI Zeolite Frameworks During Crystallization. *Angew. Chem., Int. Ed.* **2017**, *56* (19), 5164−5169.

(15) Baerlocher, C.; McCusker, L. B., Database of Zeolite Structures; http://www.iza-structure.org/databases/.

(16) Valtchev, V.; Tosheva, L. Porous Nanosized Particles: Preparation, Properties, and Applications. *Chem. Rev.* **2013**, *113* (8), 6734−6760.

(17) Chiang, H.; Bhan, A. Catalytic consequences of hydroxyl group location on the rate and mechanism of parallel dehydration reactions of ethanol over acidic zeolites. *J. Catal.* **2010**, *271* (2), 251−261.

(18) Grundner, S.; Markovits, M. A. C.; Li, G.; Tromp, M.; Pidko, E. A.; Hensen, E. J. M.; Jentys, A.; Sanchez-Sanchez, M.; Lercher, J. A. Single-site trinuclear copper oxygen clusters in mordenite for selective conversion of methane to methanol. *Nat. Commun.* **2015**, *6*, 7546.

(19) Rozanska, X.; van Santen, R. A.; Hutschka, F.; Hafner, J. A periodic DFT study of intramolecular isomerization reactions of toluene and xylenes catalyzed by acidic mordenite. *J. Am. Chem. Soc.* **2001**, *123* (31), 7655−7667.

(20) Gora-Marek, K.; Tarach, K.; Tekla, J.; Olejniczak, Z.; Kustrowski, P.; Liu, L. C.; Martinez-Triguero, J.; Rey, F. Hierarchical Mordenite Dedicated to the Fluid Catalytic Cracking Process: Catalytic Performance Regarding Textural and Acidic Properties. *J. Phys. Chem. C* **2014**, *118* (48), 28043−28054.

(21) Bhan, A.; Allian, A. D.; Sunley, G. J.; Law, D. J.; Iglesia, E. Specificity of sites within eight-membered ring zeolite channels for carbonylation of methyls to acetyls. *J. Am. Chem. Soc.* **2007**, *129* (16), 4919−4924.

(22) Boronat, M.; Martinez-Sanchez, C.; Law, D.; Corma, A. Enzyme-like Specificity in Zeolites: A Unique Site Position in Mordenite for Selective Carbonylation of Methanol and Dimethyl Ether with CO. *J. Am. Chem. Soc.* **2008**, *130* (48), 16316−16323.

(23) Vangeem, P. C.; Scholle, K.; Vandervelden, G. P. M.; Veeman, W. S. Study of the Transformation of Small-port into Large-port Mordenite by Magic Angle Spinning NMR and Infrared Spectroscopy. *J. Phys. Chem.* **1988**, *92* (6), 1585−1589.

(24) Simoncic, P.; Armbruster, T. Peculiarity and defect structure of the natural and synthetic zeolite mordenite: A single-crystal X-ray study. *Am. Mineral.* **2004**, *89* (2−3), 421−431.

(25) Pastvova, J.; Kaucky, D.; Moravkova, J.; Rathousky, J.; Sklenak, S.; Vorokhta, M.; Brabec, L.; Pilar, R.; Jakubec, I.; Tabor, E.; Klein, P.; Sazama, P. Effect of Enhanced Accessibility of Acid Sites in Micromesoporous Mordenite Zeolites on Hydroisomerization of n-Hexane. *ACS Catal.* **2017**, *7* (9), 5781−5795.

(26) Hincapie, B. O.; Garces, L. J.; Zhang, Q. H.; Sacco, A.; Suib, S. L. Synthesis of mordenite nanocrystals. *Microporous Mesoporous Mater.* **2004**, *67* (1), 19−26.

(27) Nosheen, S.; Galasso, F.; Suib, S. L. Synthesis of Mordenite Aggregates of Nanometer-Sized Crystallites. *Sci. Adv. Mater.* **2009**, *1* (1), 31−37.

(28) Ren, L. M.; Guo, Q.; Zhang, H. Y.; Zhu, L. F.; Yang, C. G.; Wang, L.; Meng, X. J.; Feng, Z. C.; Li, C.; Xiao, F. S. Organotemplate-free and one-pot fabrication of nano-rod assembled plate-like microsized mordenite crystals. *J. Mater. Chem.* **2012**, *22* (14), 6564−6567.

(29) Jo, C.; Jung, J.; Shin, H. S.; Kim, J.; Ryoo, R. Capping with Multivalent Surfactants for Zeolite Nanocrystal Synthesis. *Angew. Chem., Int. Ed.* **2013**, *52* (38), 10014−10017.

(30) Lobo, R. F.; Zones, S. I.; Davis, M. E. Structure-Direction in Zeolite Synthesis. *Journal of Inclusion Phenomena and Molecular Recognition in Chemistry* **1995**, *21* (1–4), 47–78.

(31) Corma, A.; Rey, F.; Rius, J.; Sabater, M. J.; Valencia, S. Supramolecular self-assembled molecules as organic directing agent for synthesis of zeolites. *Nature* **2004**, *431* (7006), 287–290.

(32) Xie, D.; McCusker, L. B.; Baerlocher, C.; Zones, S. I.; Wan, W.; Zou, X. D. SSZ-52, a Zeolite with an 18-Layer Aluminosilicate Framework Structure Related to That of the DeNOx Catalyst Cu-SSZ-13. *J. Am. Chem. Soc.* **2013**, *135* (28), 10519–10524.

(33) Zones, S. I.; Hwang, S. J. Synthesis of high silica zeolites using a mixed quaternary ammonium cation, amine approach: Discovery of zeolite SSZ-47. *Chem. Mater.* **2002**, *14* (1), 313–320.

(34) Camblor, M. A.; Corma, A.; Diaz-Cabanas, M. J.; Baerlocher, C. Synthesis and structural characterization of MWW type zeolite ITQ-1, the pure silica analog of MCM-22 and SSZ-25. *J. Phys. Chem. B* **1998**, *102* (1), 44–51.

(35) Turrina, A.; Garcia, R.; Watts, A. E.; Greer, H. F.; Bradley, J.; Zhou, W. Z.; Cox, P. A.; Shannon, M. D.; Mayoral, A.; Casci, J. L.; Wright, P. A. STA-20: An ABC-6 Zeotype Structure Prepared by Co-Templating and Solved via a Hypothetical Structure Database and STEM-ADF Imaging. *Chem. Mater.* **2017**, *29* (5), 2180–2190.

(36) Simoncic, P.; Armbruster, T.; Pattison, P. Cationic thionin blue in the channels of zeolite mordenite: A single-crystal X-ray study. *J. Phys. Chem. B* **2004**, *108* (45), 17352–17360.

(37) Zhang, L.; van Laak, A. N. C.; de Jongh, P. E.; de Jong, K. P. Synthesis of large mordenite crystals with different aspect ratios. *Microporous Mesoporous Mater.* **2009**, *126* (1–2), 115–124.

(38) Wu, Q. M.; Zhu, L. F.; Chu, Y. Y.; Liu, X. L.; Zhang, C. S.; Zhang, J.; Xu, H.; Xu, J.; Deng, F.; Feng, Z. C.; Meng, X. J.; Xiao, F. S. Sustainable Synthesis of Pure Silica Zeolites from a Combined Strategy of Zeolite Seeding and Alcohol Filling. *Angew. Chem., Int. Ed.* **2019**, *58* (35), 12138–12142.

(39) Berkson, Z. J.; Hsieh, M. F.; Smeets, S.; Gajan, D.; Lund, A.; Lesage, A.; Xie, D.; Zones, S. I.; McCusker, L. B.; Baerlocher, C.; Chmelka, B. F. Preferential siting of aluminum heteroatoms in the zeolite catalyst Al-SSZ-70. *Angew. Chem., Int. Ed.* **2019**, *58*, 6255–6259.

(40) Smeets, S.; Berkson, Z. J.; Xie, D.; Zones, S. I.; Wan, W.; Zou, X. D.; Hsieh, M. F.; Chmelka, B. F.; McCusker, L. B.; Baerlocher, C. Well-Defined Silanols in the Structure of the Calcined High-Silica Zeolite SSZ-70: New Understanding of a Successful Catalytic Material. *J. Am. Chem. Soc.* **2017**, *139* (46), 16803–16812.

(41) d'Espinose de la Caillerie, J. B.; Fretigny, C.; Massiot, D. MAS NMR spectra of quadrupolar nuclei in disordered solids: The Czjzek model. *J. Magn. Reson.* **2008**, *192* (2), 244–251.

(42) Anderson, M. W.; Barrie, P. J.; Klinowski, J. H-1 Magic-Angle-Spinning NMR-Studies of the Adsorption of Alcohols on Molecular-Sieve Catalysts. *J. Phys. Chem.* **1991**, *95* (1), 235–239.

(43) Qin, W.; Jain, R.; Hernandez, F. C. R.; Rimer, J. D. Organic-Free Interzeolite Transformation in the Absence of Common Building Units. *Chem. - Eur. J.* **2019**, *25* (23), 5893–5898.

(44) Kumar, M.; Luo, H.; Roman-Leshkov, Y.; Rimer, J. D. SSZ-13 Crystallization by Particle Attachment and Deterministic Pathways to Crystal Size Control. *J. Am. Chem. Soc.* **2015**, *137* (40), 13007–13017.

(45) Choi, M.; Na, K.; Kim, J.; Sakamoto, Y.; Terasaki, O.; Ryoo, R. Stable single-unit-cell nanosheets of zeolite MFI as active and long-lived catalysts. *Nature* **2009**, *461* (7261), 246–U120.

(46) Li, X. F.; Prins, R.; van Bokhoven, J. A. Synthesis and characterization of mesoporous mordenite. *J. Catal.* **2009**, *262* (2), 257–265.

(47) Garaga, M. N.; Hsieh, M. F.; Nour, Z.; Deschamps, M.; Massiot, D.; Chmelka, B. F.; Cadars, S. Local environments of boron heteroatoms in non-crystalline layered borosilicates. *Phys. Chem. Chem. Phys.* **2015**, *17* (33), 21664–21682.

(48) Lesage, A.; Sakellariou, D.; Steuernagel, S.; Emsley, L. Carbon-proton chemical shift correlation in solid-state NMR by through-bond multiple-quantum spectroscopy. *J. Am. Chem. Soc.* **1998**, *120* (50), 13194–13201.

(49) Van Veenendaal, E.; Meier, B. H.; Kentgens, A. P. M. Frequency stepped adiabatic passage excitation of half-integer quadrupolar spin systems. *Mol. Phys.* **1998**, *93* (2), 195–213.

(50) Elena, B.; de Paepe, G.; Emsley, L. Direct spectral optimization of proton-proton homonuclear dipolar decoupling in solid-state NMR. *Chem. Phys. Lett.* **2004**, *398* (4–6), 532–538.

(51) Fung, B. M.; Khitrin, A. K.; Ermolaev, K. An improved broadband decoupling sequence for liquid crystals and solids. *J. Magn. Reson.* **2000**, *142* (1), 97–101.

(52) Willmott, P. R.; Meister, D.; Leake, S. J.; Lange, M.; Bergamaschi, A.; Boge, M.; Calvi, M.; Cancellieri, C.; Casati, N.; Cervellino, A.; Chen, Q.; David, C.; Flechsig, U.; Gozzo, F.; Henrich, B.; Jaggi-Spielmann, S.; Jakob, B.; Kalichava, I.; Karvinen, P.; Krempasky, J.; Ludeke, A.; Luscher, R.; Maag, S.; Quitmann, C.; Reinle-Schmitt, M. L.; Schmidt, T.; Schmitt, B.; Streun, A.; Vartiainen, I.; Vitins, M.; Wang, X.; Wullschleger, R. The Materials Science beamline upgrade at the Swiss Light Source. *J. Synchrotron Radiat.* **2013**, *20*, 667–682.

(53) Hess, B.; Kutzner, C.; van der Spoel, D.; Lindahl, E. GROMACS 4: Algorithms for highly efficient, load-balanced, and scalable molecular simulation. *J. Chem. Theory Comput.* **2008**, *4* (3), 435–447.

(54) Cygan, R. T.; Liang, J. J.; Kalinichev, A. G. Molecular models of hydroxide, oxyhydroxide, and clay phases and the development of a general force field. *J. Phys. Chem. B* **2004**, *108* (4), 1255–1266.

(55) Wang, J. M.; Wolf, R. M.; Caldwell, J. W.; Kollman, P. A.; Case, D. A. Development and testing of a general amber force field (vol 25, pg 1157, 2004). *J. Comput. Chem.* **2005**, *26* (1), 114–114.

(56) Frenkel, D.; Smit, B. *Understanding molecular simulation: from algorithms to applications*, 2nd ed.; Academic Press: San Diego, CA, 2002.

(57) Bussi, G.; Donadio, D.; Parrinello, M. Canonical sampling through velocity rescaling. *J. Chem. Phys.* **2007**, *126* (1), 014101.

(58) Parrinello, M.; Rahman, A. Polymorphic Transitions in Single-Crystals - a New Molecular-Dynamics Method. *J. Appl. Phys.* **1981**, *52* (12), 7182–7190.

(59) Chawla, A.; Li, R.; Jain, R.; Clark, R. J.; Sutjianto, J. G.; Palmer, J. C.; Rimer, J. D. Cooperative effects of inorganic and organic structure-directing agents in ZSM-5 crystallization. *Mol. Syst. Des. Eng.* **2018**, *3* (1), 159–170.

(60) Kim, S. B.; Palmer, J. C.; Debenedetti, P. G. A Computational Study of the Effect of Matrix Structural Order on Water Sorption by Trp-Cage Miniproteins. *J. Phys. Chem. B* **2015**, *119* (5), 1847–1856.

(61) Davis, T. M.; Liu, A. T.; Lew, C. M.; Xie, D.; Benin, A. I.; Elomari, S.; Zones, S. I.; Deem, M. W. Computationally Guided Synthesis of SSZ-52: A Zeolite for Engine Exhaust Clean-up. *Chem. Mater.* **2016**, *28* (3), 708–711.

(62) Pophale, R.; Daeyaert, F.; Deem, M. W. Computational prediction of chemically synthesizable organic structure directing agents for zeolites. *J. Mater. Chem. A* **2013**, *1* (23), 6750–6760.

(63) Hwang, A.; Prieto-Centurion, D.; Bhan, A. Isotopic tracer studies of methanol-to-olefins conversion over HSAPO-34: The role of the olefins-based catalytic cycle. *J. Catal.* **2016**, *337*, 52–56.

Supporting Information for

Crystallization of Mordenite Platelets using Cooperative Organic Structure-Directing Agents

Manjesh Kumar[1], Zachariah J. Berkson[2], R. John Clark[1], Yufeng Shen[1], Nathan A. Prisco[2], Qi Zheng[3], Zhiyuan Zeng[3,4], Haimei Zheng[3,4], Lynne B. McCusker[2,5], Jeremy C. Palmer[1], Bradley F. Chmelka[2,*], and Jeffrey D. Rimer[1,*]

[1]Department of Chemical and Biomolecular Engineering, University of Houston, 4726 Calhoun Road, Houston, TX, 77204, USA

[2]Department of Chemical Engineering, University of California, Santa Barbara, Santa Barbara, CA, 93106, USA

[3]Materials Sciences Division, Lawrence Berkeley National Laboratory, Berkley, 1 Cyclotron Road, CA, 94720, USA

[4]Department of Materials Science and Engineering, University of California, Berkley, CA, 94720, USA

[5]Department of Materials, ETH Zurich, Vladimir-Prelog-Weg 5, CH-8093 Zurich, Switzerland

*Correspondence sent to. jrimer@central.uh.edu and bradc@engineering.ucsb.edu

Supporting Information Materials

Experimental and Computational Methods

Tables S1 to S4

Figures S1 to S27

Movie S1

Experimental and Computational Methods

Synchrotron X-ray powder diffraction (XPD) analysis

In the hope that the arrangement of the sodium and organic species within the pores of the mordenite framework structure could be discerned experimentally, synchrotron powder diffraction data were collected. Analysis of the data revealed the presence of a quartz impurity, so a 2-phase refinement using the program TOPAS (A.A. Coelho, TOPAS-ACADEMIC v5.0; 2012) was undertaken. Idealized structures for the two OSDA species were generated using the program Avogadro (version 1.2.0).[1]

For the quartz phase, the published structure[2] was used and only the peakshape parameters and scale factor were refined. For the mordenite phase, structure analysis was initiated using the known **MOR**-type framework structure[3] in the highest symmetry space group (*Cmcm*). A drawing of the mordenite framework structure and its main features is shown in Figure S1. The pattern was scaled using only the high-angle data and then a difference electron density (DED) map was generated using the complete pattern. This showed a significant column of electron density in the middle of the 12-ring channel. As the width of this column had a diameter consistent with that of the TMAda$^+$ molecule, a simulated annealing (SA) global optimization procedure for locating organic species in zeolites[4] was applied to find the best location and orientation of a rigid TMAda$^+$ molecule within this electron density. A second DED map revealed the positions of the Na$^+$ ions in the center of the oval 8-ring channels, where they coordinate to six framework oxygen atoms. The next DED map showed electron density in the 8-ring side pocket of the 12-ring channel, so the SA procedure was applied once again, this time searching for the best position of the head group (C_2O_2) of the $D6_{1,2}$ molecule. The final DED map showed a peak distinct from the diol O atom that was within bonding distance of the Na$^+$ ion, so this was interpreted as a water molecule.

This approximate model was then refined to yield the structure shown in Figure S13 and the profile fit shown in Figure S8. Because NMR results showed that ca. 1/3 of the TMAda$^+$ cations were in fact neutral dimethyladamantine (DMAda) molecules, the occupancy parameters of the methyl groups were adjusted accordingly. Geometric restraints were applied to the zeolite framework structure and the $D6_{1,2}$ head group for structure refinement. The TMAda$^+$/DMAda species were treated as a rigid body and only the occupancy, position, orientation and the torsion angle around the N1-C4 bond were refined. Refinement including the quartz phase converged with the R-values given in Table S4.

The TMAda$^+$/DMAda species are centered in the 12-ring channel and tilted with respect to the crystallographic *c* axis by approximately 20°. There are two entities per unit cell (one per 12-ring channel). The two Na$^+$ ions per unit cell are located at the center of the tilted 8-rings that form the oval 8-ring channel. Each is coordinated to six framework O atoms, one $D6_{1,2}$ O atom and one water molecule. Only the C_2O_2 head group of the $D6_{1,2}$ molecule could be located. This probably reflects the fact that the tail is extremely flexible and probably disordered over many different sites. Because the O atom of the terminal OH group interacts with Na$^+$ ions and the second OH group can form a hydrogen bond with framework O atoms, their positions are better defined and therefore visible in the DED map. The disordered tail appears to go through the 8-ring side pocket towards the 12-ring channel.

Minimization of quartz impurity

Excess silica in the HOU-4 reaction mixture results in the formation of a dense and inert quartz phase and a minor unidentified aluminosilicate phase as detected by synchrotron XPD (Figures

1D and S8). The quartz byproduct identified in HOU-4 is a commonly reported impurity in zeolite synthesis.[5, 6] The formation of quartz from growth solution C1 is attributed to a higher silica concentration that is more common for syntheses of SSZ-13 and ZSM-5, compared to less siliceous growth mixtures used to prepare conventional mordenite (e.g. growth solution C5 in Table S1). In order to reduce the quartz content in HOU-4, the composition of the growth mixture was varied by first increasing the $D6_{1,2}$ concentration and then decreasing the quantity of silica (Figures S21 and S22). Additional modifications, such as the reduction of water content (Figure S21), had a negligible impact on product purity. Collectively, the changes made to the growth mixture improved the purity of HOU-4, but they were unable to remove the quartz phase completely. It should be noted that the presence of quartz in the H-HOU-4 catalyst used for cumene cracking (Figure 8) is accounted for in the calculation of TON through NH_3 TPD measurements of total acid density.

Additional discussion of solid-state NMR results

Molecular-level insights into the Al heteroatom distribution and framework-OSDA interactions in HOU-4 are provided by solid-state two-dimensional (2D) heteronuclear correlation MAS NMR spectra. Solid-state 2D NMR correlation spectra exploit internuclear dipole-dipole (through-space) or J (through-covalent-bond) couplings and are plotted as 2D contour plots, where correlated signal intensities indicate the mutual proximities or covalent connectivities of the corresponding ^1H, ^{13}C, ^{27}Al, or ^{29}Si species.[7, 8] The covalently bonded ^{27}Al-O-^{29}Si framework moieties in HOU-4 are unambiguously established by the 2D $^{27}Al\{^{29}Si\}$ J-mediated NMR correlation spectrum (Figure 5A), which selectively detects ^{27}Al-^{29}Si nuclear spin pairs that are J coupled through covalent ^{27}Al-O-^{29}Si bonds. The 2D spectrum shows a single ^{27}Al signal at 54 ppm from tetrahedral framework aluminum sites, which is correlated to ^{29}Si signals at -109 to -102 ppm from fully crosslinked Q^4(1Al) ^{29}Si species and at -99 ppm from partially crosslinked Q^3(1Al) ^{29}Si species. (Q^m(nAl) denotes a tetrahedral Si atom that is bonded through bridging oxygen atoms to m Si or Al atoms, of which n are Al.) Previously, such 2D $^{27}Al\{^{29}Si\}$ through-bond J-mediated correlation spectra of aluminosilicate zeolites have been challenging to obtain due in part to the low natural isotopic abundance of ^{29}Si (4.7%) and the weak ^{27}Al-O-^{29}Si J couplings (<20 Hz), but are enabled here by the improved sensitivity provided by low-temperature (95 K) measurement conditions. The ^{27}Al signals exhibit Czjzek lineshapes[9] that reflect a random distribution of ^{27}Al heteroatom environments within the mordenite framework and among the four distinct tetrahedral (T) sites. This is corroborated by complementary ^{27}Al triple-quantum MAS NMR analyses of the same HOU-4 sample (Figure S17). The relatively small percentage of partially-crosslinked Q^3 species (*ca.* 2%, Figure S18) are likely associated with defect sites at the exterior particle surfaces of the ultrathin HOU-4 crystallites.

The site-specific interactions of the different framework ^{27}Al species with OSDA molecules are established by 2D $^{27}Al\{^1H\}$ and $^{13}C\{^1H\}$ dipolar-mediated HETeronuclear CORrelation (HETCOR) NMR spectra (Figure 5B and C). The 2D HETCOR spectra yield correlated ^{13}C- or ^{27}Al-^1H signal intensities from ^{13}C-^1H or ^{27}Al-^1H nuclear spin pairs that are dipole-dipole coupled through space over distances of <1 nm. The different ^1H signals are assigned to the different ^1H moieties on $D6_{1,2}$ (green shaded regions) or $TMAda^+$ (red shaded regions) OSDA molecules on the basis of the 2D $^{13}C\{^1H\}$ HETCOR NMR spectrum of HOU-4 acquired with a very short contact time (0.5 ms, Figure S10).

Different types of tetrahedrally-coordinated framework aluminum sites within the mordenite zeolite framework are distinguished on the basis of their interactions with the different OSDA

molecules, as manifested by the 2D ^{27}Al{^{1}H} HETCOR spectrum in Figure 5B. Specifically, the ^{27}Al signal at 55 ppm from tetrahedrally-coordinated ^{27}Al is correlated with ^{1}H signals at 2.2 ppm and 2.6-3.1 ppm from alkyl D6$_{1,2}$ and TMAda$^+$ moieties, respectively, indicating the mutual nanoscale proximities of the corresponding ^{27}Al species to both types of OSDA molecules. These correlated intensities are consistent with the TMAda$^+$ molecules acting as charge-balancing cations for the negative charges associated with the framework ^{27}Al heteroatom sites. As the TMAda$^+$ molecules are too large to occupy the 8-membered ring channels in the mordenite zeolite structure and must be situated within the 12-membered ring channels, the ^{27}Al signal at 55 ppm corresponds to ^{27}Al heteroatom sites within the 12-membered ring channels. Interestingly, ^{27}Al signals at 53 and 55 ppm are both also correlated with an additional ^{1}H signal at 3.6 ppm, which arises from the -OH moieties on the D6$_{1,2}$ molecules (Figure S10). The 3.6 ppm ^{1}H chemical shift of the D6$_{1,2}$ -OH moieties is characteristic of the coordination of the alcohol -OH moieties to Na$^+$ cations that balance the negative framework charges,[10] as depicted schematically in Figure 5D. This signal assignment is corroborated by the 2D ^{23}Na{^{1}H} HETCOR spectrum in Figure S20, which shows correlations between a ^{23}Na signal at -9 ppm from Na$^+$ cations and partially-resolved ^{1}H signals at 2.2, 3.6, and 4.7 ppm, which are assigned respectively to C-H moieties on D6$_{1,2}$ molecules, -OH moieties on D6$_{1,2}$ molecules, and adsorbed H$_2$O. Within the detection limits of the NMR measurements, the ^{27}Al signal at 53 ppm is not correlated to ^{1}H signals from TMAda$^+$ molecules, indicating that the corresponding ^{27}Al species are not proximate (within ~0.5 nm for the short contact time used for the 2D ^{27}Al{^{1}H} HETCOR spectrum) to TMAda$^+$ molecules. On the basis of the synchrotron XPD analysis, the Na$^+$ cations are sited primarily within the 8-membered ring channels. The 2D ^{27}Al{^{1}H} HETCOR spectrum thus establishes the presence of two different types of ^{27}Al species: those charge-balanced by TMAda$^+$ headgroups within the 12-membered ring channels and those charge-balanced by Na$^+$ cations complexed with D6$_{1,2}$ -OH moieties, which are within the 8-membered ring channels. Complementary 2D ^{29}Si{^{1}H} HETCOR analyses of HOU-4 support these conclusions and additionally show that the hydrophobic regions of the TMAda$^+$ and D6$_{1,2}$ OSDA molecules interact with siliceous Q^4(0Al) and Q^4(1Al) ^{29}Si species within the zeolite framework (Figure S21).

The different TMAda$^+$ and D6$_{1,2}$ OSDA molecules are intimately commingled and interact with each other within the mordenite zeolite framework, as determined by analysis of the 2D ^{13}C{^{1}H} HETCOR spectrum of HOU-4 in Figure 5C. The 2D ^{13}C{^{1}H} HETCOR spectrum shows correlated signal intensities from intramolecular interactions of ^{1}H and ^{13}C moieties on the D6$_{1,2,}$ molecules (green shaded regions) and on the TMAda$^+$ molecules (red shaded regions). Additionally, the ^{13}C signals at 15, 24, 28, 34, 67, and 73 ppm from the six different ^{13}C atoms on the D6$_{1,2}$ molecules are each correlated with ^{1}H signals in the 2.6-3.3 ppm range, which arise from ^{1}H moieties on the TMAda$^+$ molecules (purple shaded regions). These correlated signal intensities establish unambiguously that D6$_{1,2}$ and TMAda$^+$ OSDA molecules interact with each other over nanoscale distances (<1 nm) within the mordenite zeolite nanochannels. We conclude that the different types of OSDA molecules are aggregated within the zeolite nanopores and likely act in tandem during the hydrothermal crystallization of the zeolite framework to direct the formation and stabilization of the large linear 12-membered rings that comprise the mordenite nanochannel system.

Presence of N,N-dimethyladamantamine in HOU-4

N,N-dimethyladamantamine (DMAda) forms from partial decomposition of TMAda$^+$ and is occluded within HOU-4. This is evidenced by the solid-state 1D ^{13}C MAS NMR spectrum of

HOU-4 in Figure S14, which shows ^{13}C signals at 15, 23, 29, 34, 67, and 73 ppm from 1,2-hexanediol as well as 31, 49, and 78 ppm from TMAda$^+$. Additional weak ^{13}C signals at 46 and 58 ppm are assigned to ^{13}C species in DMAda [11], consistent with the hydrothermal degradation of TMAda$^+$ via Hofmann elimination [12]. The quantitative ^{13}C NMR analysis indicates an approximate molar ratio of 1 DMAda : 2 TMAda$^+$ in HOU-4. DMAda is also present in the HOU-4 synthesis mixture, as established by the ^{13}C signals at 54, 44, 35, and 31 ppm in the solution-state 1D ^{13}C NMR spectrum of the synthesis mixture effluent in Figure S19. While DMAda and TMAda$^+$ cannot be distinguished in the synchrotron XPD analyses because of their similar molecular architectures, it is likely that DMAda and TMAda$^+$ occupy the same positions within the linear 12-ring mordenite channels in HOU-4. The removal of a methyl group on TMAda$^+$ would allow the alkyl tail of hexanediol, which may protrude into the 12-ring channels, to be accommodated more easily.

Method of simulated diffraction patterns

Simulated diffraction patterns were calculated by Single Crystal 2.3.3[13] based on the mordenite (**MOR**) framework from the database of zeolites structures.[14] In our simulation, the spot size was set to 0.02 Å^{-1} with 100% intensity saturation. The beam voltage was 200 keV with the electron wavelength reaching to 0.025 Å. In addition, the crystal thickness normal to the radiation beam was 60 nm, which was consistent with the dimensions from AFM measurements (Figure 2B). As default, the beam convergence was 1.0º and the Gamma correction was 2.2.

Supporting Tables

Table S1. Synthesis conditions used to prepare zeolites

Sample	Molar Composition of Growth Mixture						T (°C)	Time (d)	Zeolite Structure
	$Al(OH)_3$	SiO_2	NaOH	H_2O	TMAdaOH	$D6_{1,2}$			
C1	0.052	1.0	0.2	44	0.1	1.6	180	6	HOU-4[a]
C2	0.052	1.0	0.2	44	0.1	0.0	180	6	SSZ-13
C3	0.052	1.0	0.2	44	0.0	1.6	180	6	ZSM-5
C4	0.052	1.0	0.2	44	0.0	0.0	180	6	ZSM-5
C5	2.0	30	12	775	0.0	0.0	170	4	MOR

(a) Contains quartz impurity (see Figure S6)

Table S2. Elemental analysis and acidity of zeolite frameworks

Sample	Si/Al (EDX)	Si/Al (ICP)	NH_3-TPD (µmol/g)
HOU-4	9.5	16.0 [a]	345
MOR	8.0	7.7	974
SSZ-13	11.6	----	----
ZSM-5	11.7	----	----

(a) Sample contains quartz impurity (see Figure S6)

Table S3. Framework OSDA per unit cell based on TGA analysis of washed samples

Zeolite	Framework	Unit cell	Molecular wt / unit cell	% weight loss	SDA/unit cell
SSZ-13	CHA	$Na_3Al_3Si_{33}O_{72}$	2228.52	10	1.3 $TMAda^+$
ZSM-5	MFI	$Na_8Al_8Si_{88}O_{192}$	5942.72	5	2.7 $D6_{1,2}$
HOU-4	MOR	$Na_5Al_5Si_{43}O_{96}$	2993.24	3.5	0.6 $TMAda^{+}$ [a]
				37	------ [b]

(a) Analysis of unwashed samples by ^{13}C NMR analysis reveals 1.1 - 1.5 $TMAda^+$ and 0.6 - 0.8 DMAda per unit cell (total of 1.7 - 2.3 $TMAda^+$/DMAda per unit cell). PXRD analysis estimates 2 $TMAda^+$ per unit cell, but cannot distinguish between $TMAda^+$ and DMAda. (b) Thermogravimetric analysis of unwashed sample contains organics within zeolite pores and on exterior surfaces, rendering the determination of SDA/per unit cell difficult [This work was supported, in part, by the State of Texas through the Texas Center for Superconductivity at the University of Houston]

Table S4. Crystallographic details for the refinement of the structure of HOU-4.

Sample	HOU-4
Chemical composition	$|Na_2(C_{13}H_{24}N)_{1.2}(C_{12}H_{21}N)_{0.6}(C_6H_{14}O_2)_{1.9}(H_2O)_2|[Al_{3.2}Si_{44.8}O_{96}]$
Space group	*Cmcm*
a (Å)	17.9875(2)
b (Å)	20.4609(3)
c (Å)	7.4826(1)
V (Å³)	2754
λ (Å)	0.70847(1)
2θ range (°)	2.7–39.8
HOU-4 : Quartz (wt %)	62.5:37.5
HOU-4 R_I	0.097
Quartz R_I	0.050
R_{wp}	0.235
R_{exp}	0.009
Observations	10298
Reflections (HOU-4)	763
Parameters	31 (framework)
	13 (D6$_{1,2}$, water)
	8 (TMAda⁺/DMAda)
	13 (profile)
	7 (quartz)
Geometric restraints	44 (framework)
	6 (D6$_{1,2}$)
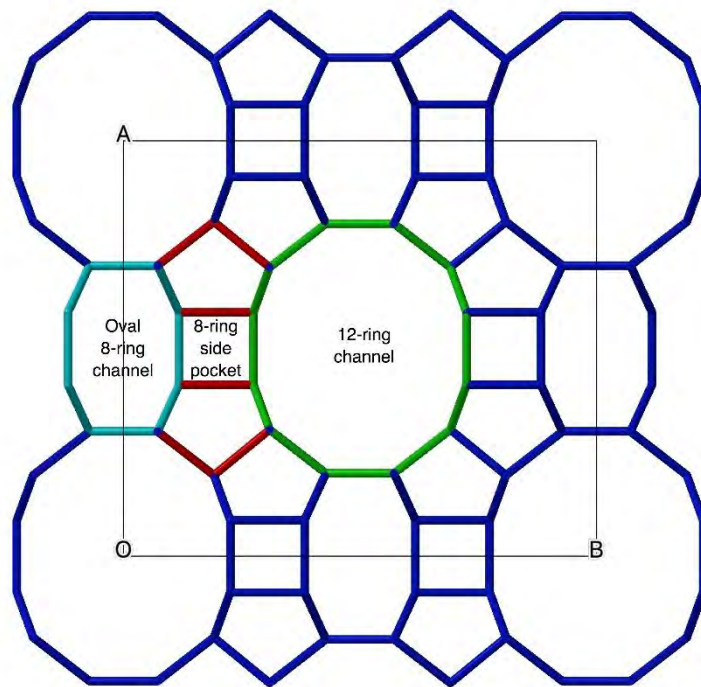
Figure S1. The **MOR**-type framework structure showing the arrangement of the 12-ring channels, their 8-ring side pockets, and the parallel oval 8-ring channels.
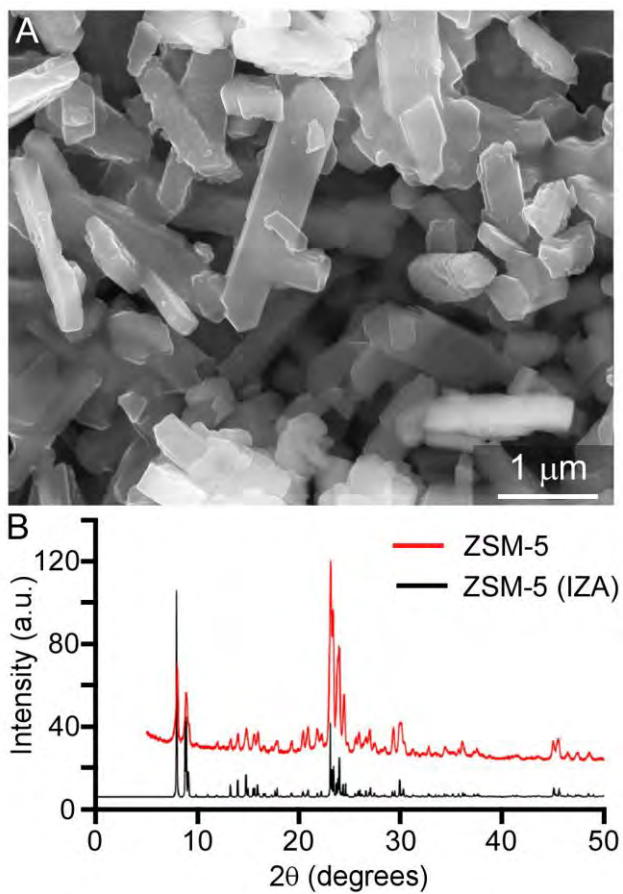
Figure S2. (A) Electron micrograph of ZSM-5 crystals obtained from a growth mixture with molar composition C4 (Table S1). (B) X-ray powder diffraction pattern of as-made ZSM-5 crystals (red marked) synthesized without organic (i.e., sodium was used as an inorganic structure-directing agent).
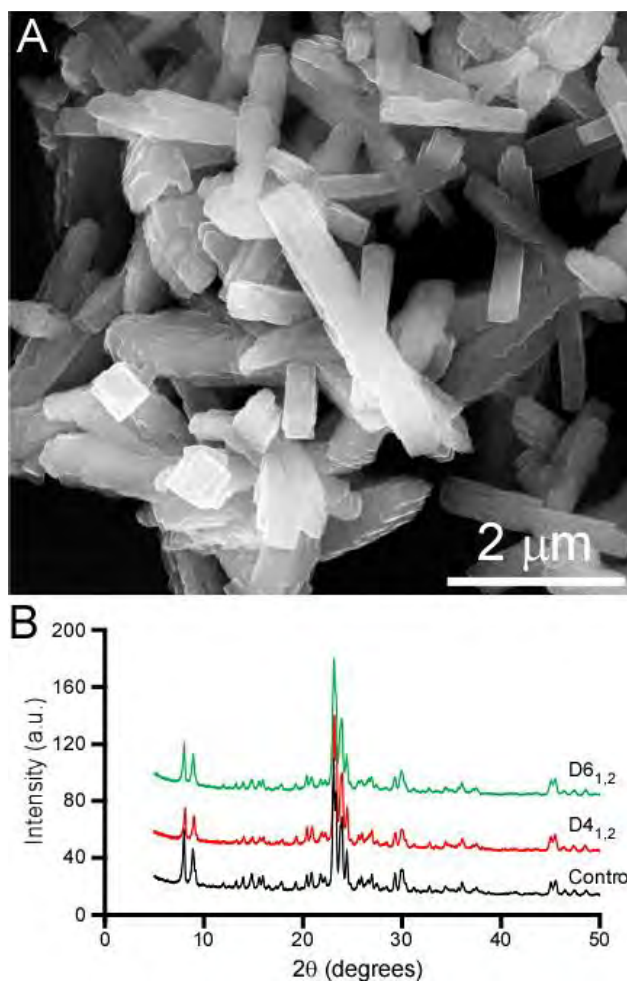
Figure S3. (A) Electron micrograph of ZSM-5 crystals synthesized in the presence of 1.6 $D4_{1,2}$: 1.0 SiO_2. (B) Powder X-ray diffraction patterns of as-made products without alcohols (*control*: black, solution C4) and those in the presence of $D6_{1,2}$ (green, solution C3) and $D4_{1,2}$ (red, modified solution C3).
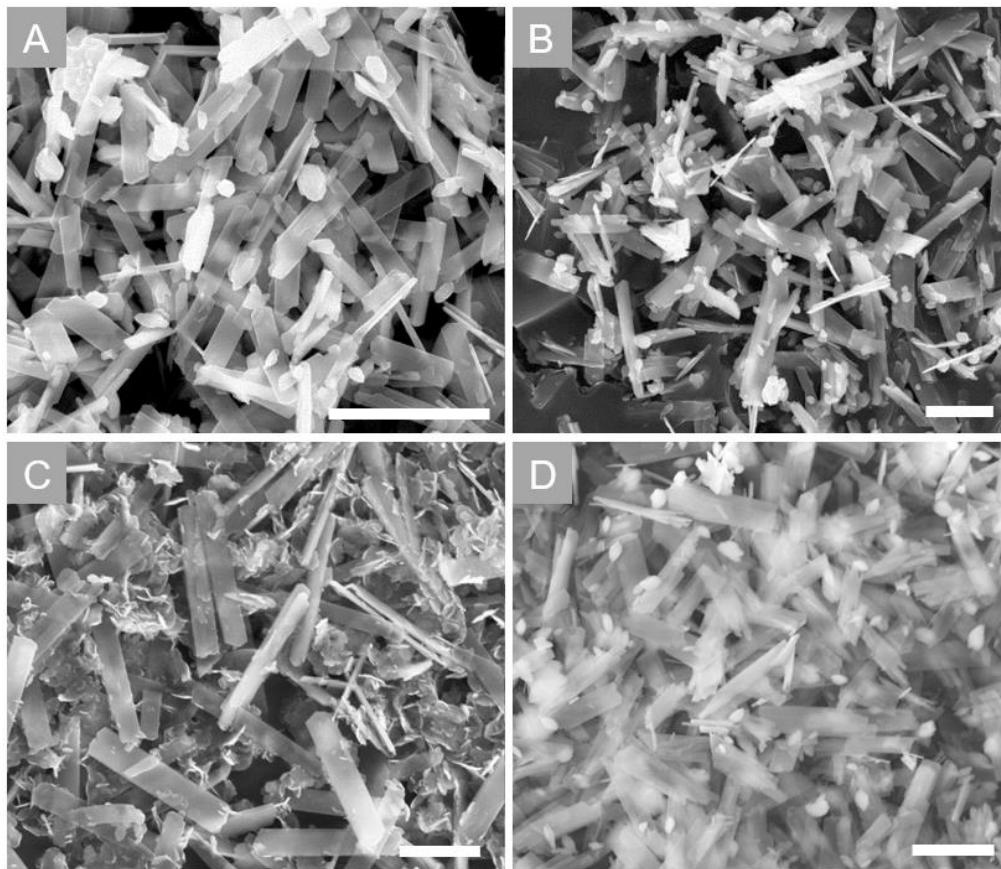
Figure S4. (A – D) Representative low-resolution scanning electron micrographs of HOU-4 samples prepared from four separate batches using growth solution C1. The scale bars are equal to 5 μm.
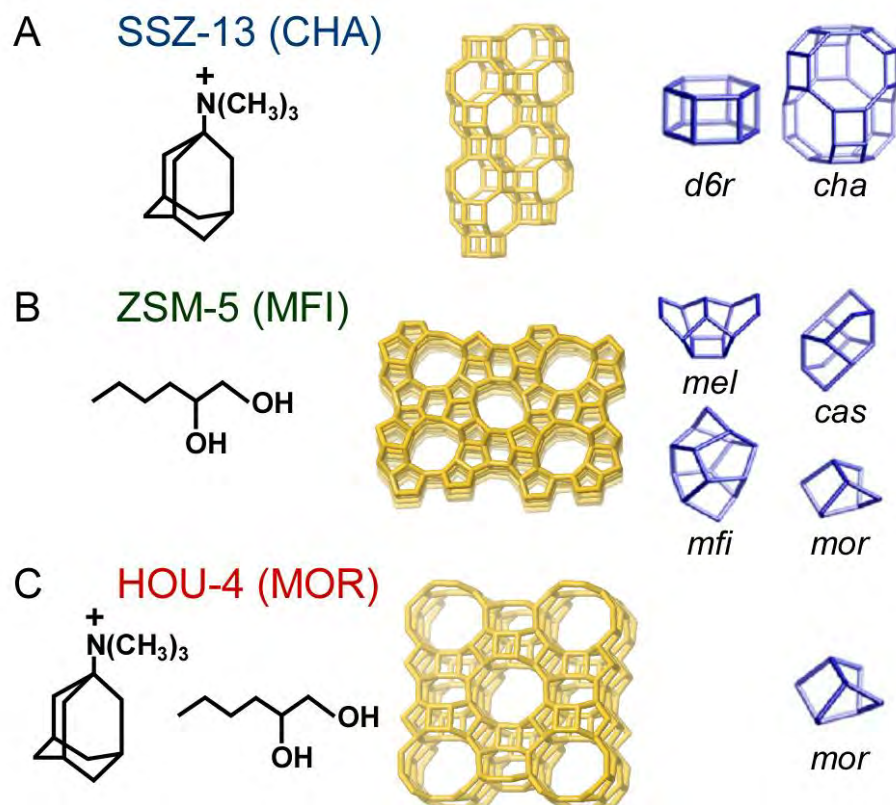
Figure S5. The OSDA(s) (left column), corresponding zeolite structure (middle column), and composite building units (right column)[14] for (A) SSZ-13 (CHA), (B) ZSM-5 (MFI), and (C) HOU-4 (**MOR**).
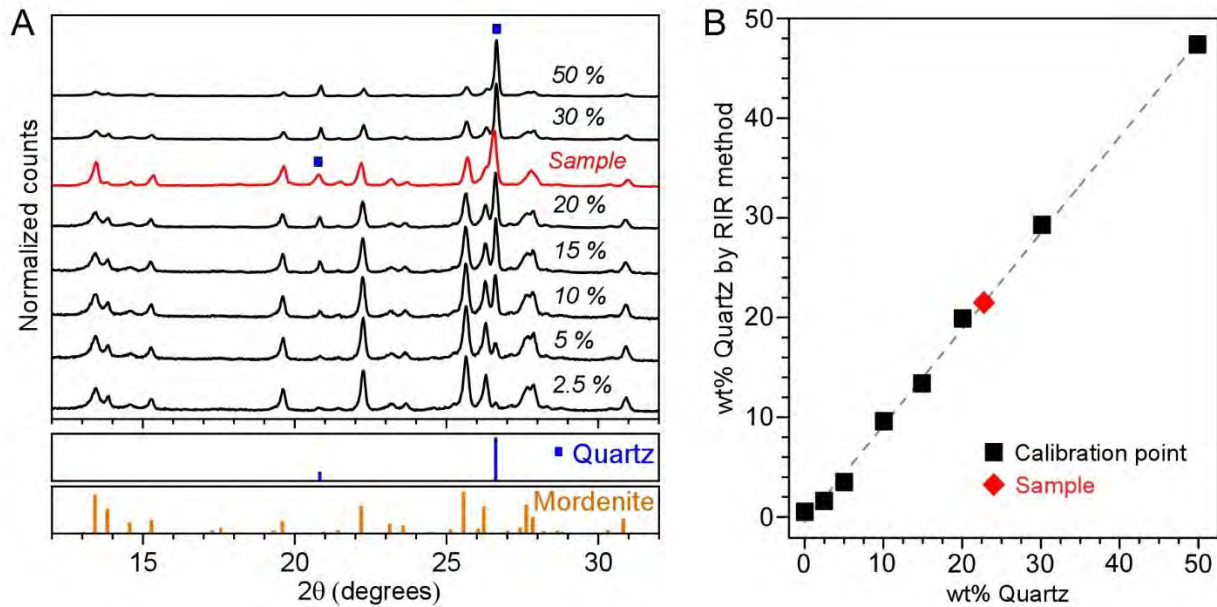
Figure S6. Quantitative Reference Intensity Ratio (RIR) analysis was performed using (A) a series of XPD patterns of physically mixed mordenite-quartz reference mixtures of increasing quartz weight percent, followed by (B) interpolation of the sample (HOU-4, indicated in red) on the corresponding calibration curve. Analysis performed using the Integrated Powder X-ray Diffraction Software PDXL 2.2 (Rigaku Corporation), using mordenite (Zeolyst Int., CBV 10A) and ground white quartz sand (Sigma Aldrich) as reference materials. Mordenite (ICDD 01-081-8072, RIR = 0.65) and quartz (ICDD 01-085-0930, RIR = 3.15) were used as reference patterns. For the HOU-4 sample, the estimated weight percentage of quartz by the RIR method is 22 wt% (interpolated: 23 wt%).
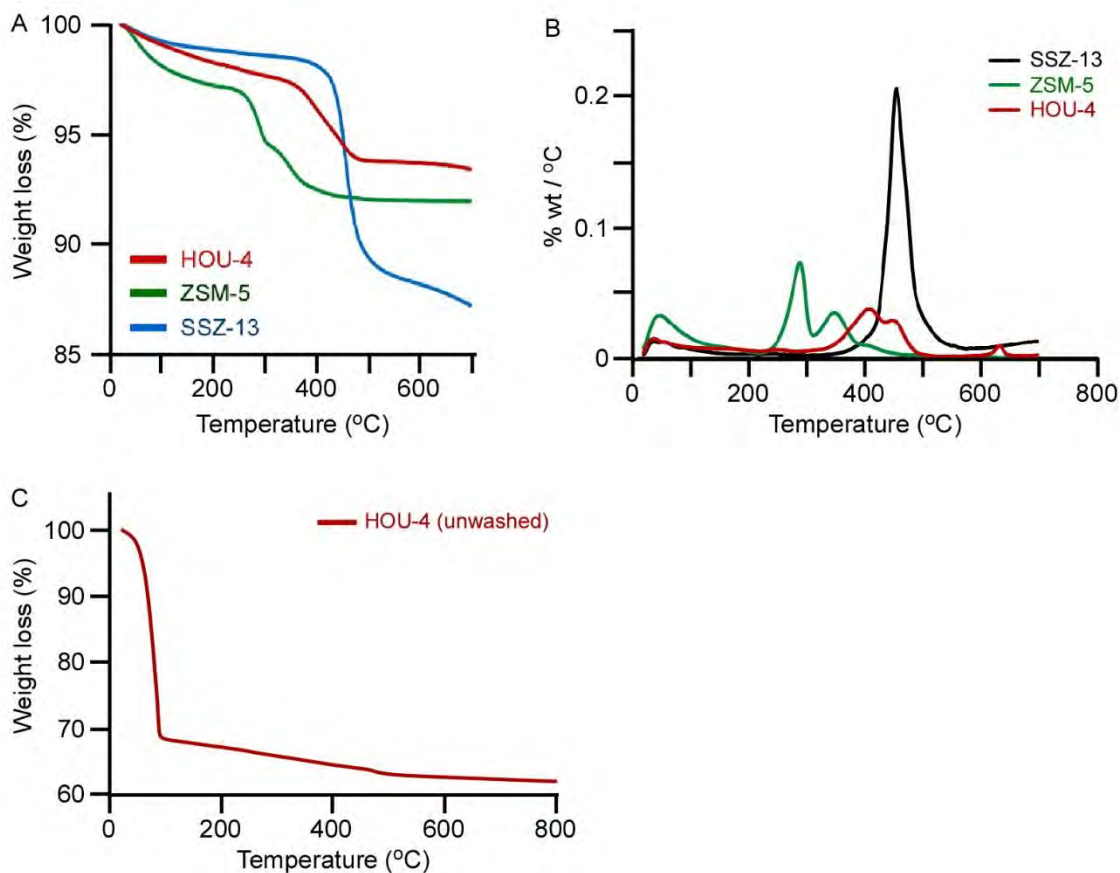
Figure S7. (A) Thermogravimetric analysis (TGA) of washed SSZ-13 (blue), ZSM-5 (green), and HOU-4 (red) samples. (B) Derivative weight loss as function of ramp up temperature in TGA. The graphs correspond to the following samples synthesized using the compositions listed in Table S1: (black) SSZ-13 prepared with solution C2; (green) ZSM-5 prepared with solution C3; and (red) HOU-4 prepared with solution C1. (C) TGA of an unwashed HOU-4 sample.
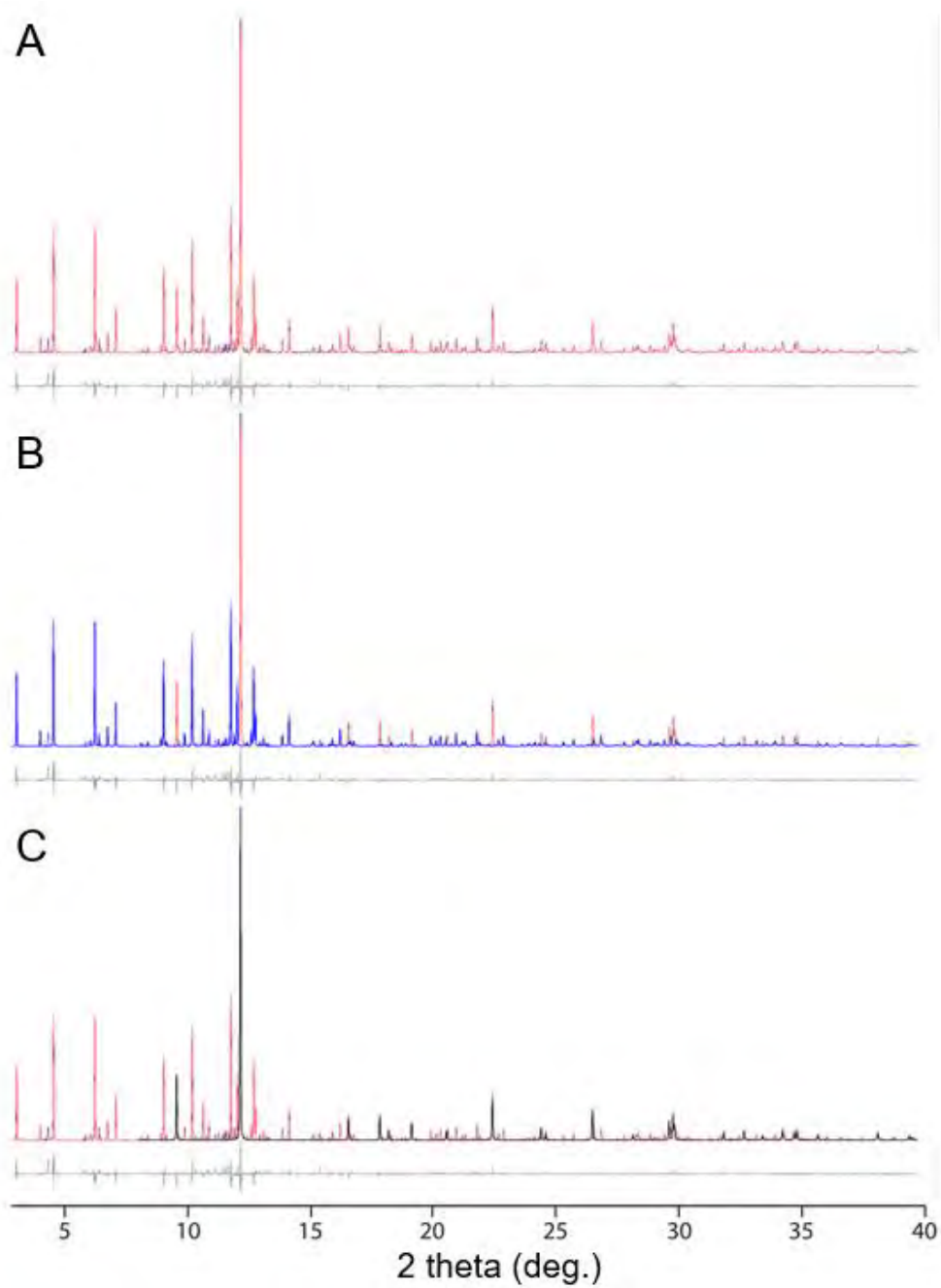
Figure S8. (A) Synchrotron XPD data displayed as the measured (blue), calculated (red), and difference profiles (gray) for the Rietveld refinement of the structure of HOU-4 with the quartz impurity included as a second phase. The contribution from HOU-4 is highlighted in blue in (B) and that from quartz in black in (C).
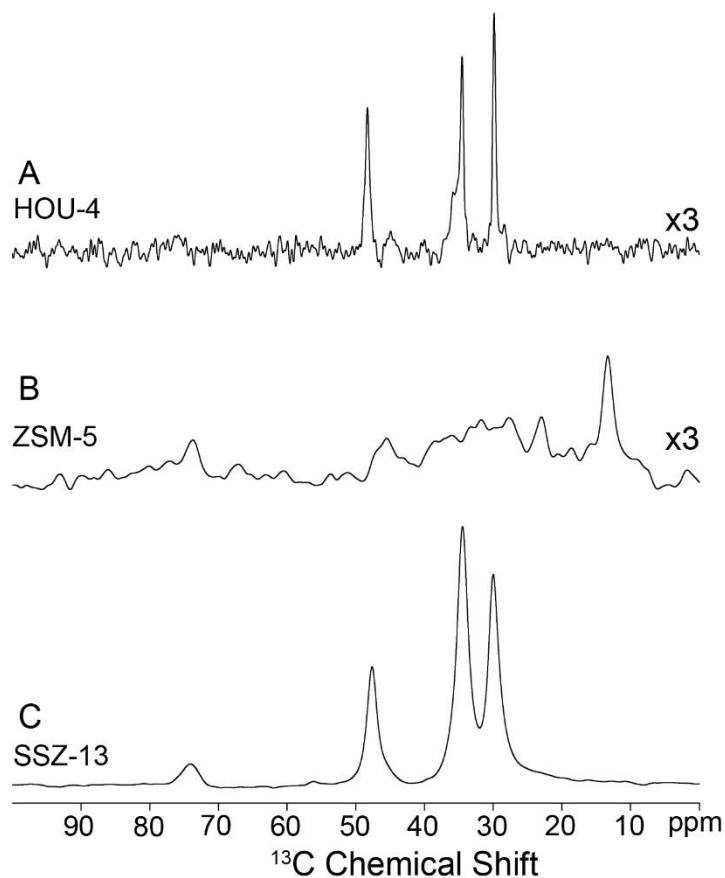
Figure S9. Solid-state 1D $^{13}C\{^{1}H\}$ CPMAS spectra of (A) washed as-made HOU-4 synthesized with TMAda$^+$ and D6$_{1,2}$ as dual OSDAs, (B) washed ZSM-5 synthesized with D6$_{1,2}$ as the OSDA, and (C) washed SSZ-13 synthesized with TMAda$^+$ as the OSDA. The spectra were acquired at 11.7 T, 10 kHz MAS, 298 K, and with contact times of 2 ms. The spectrum in (A) shows only signals from TMAda$^+$ molecules, consistent with the removal of D6$_{1,2}$ molecules by the post-synthesis washing.
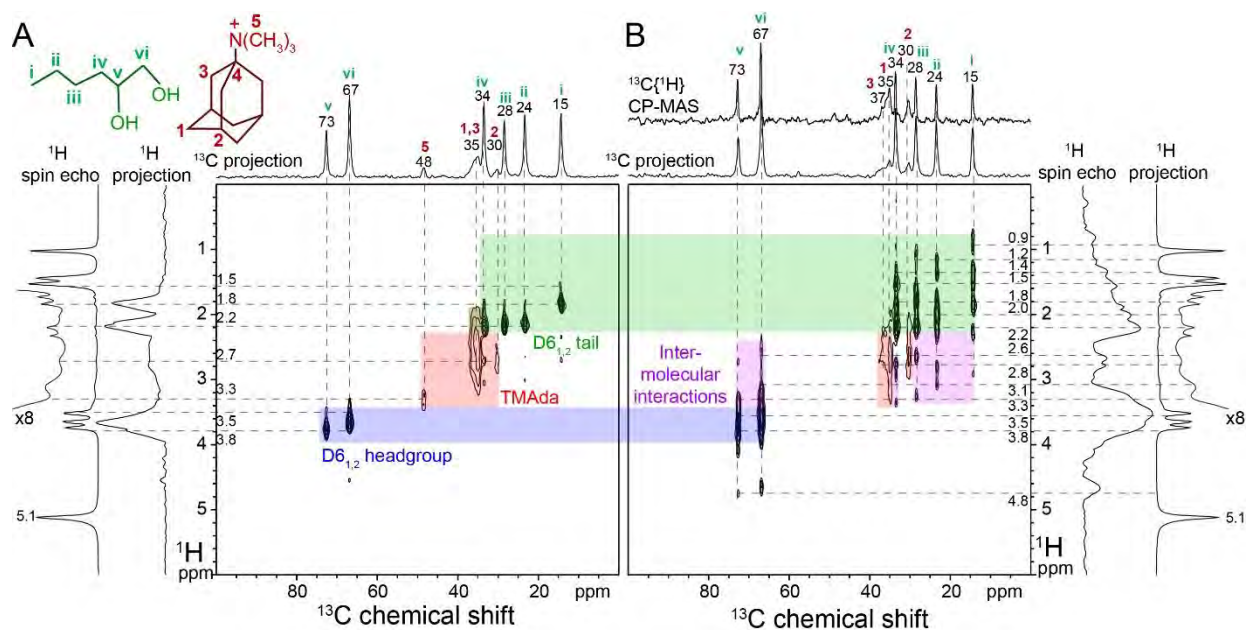
Figure S10. Solid-state 2D ^{13}C{^{1}H} correlation spectra of as-made HOU-4 (same sample as Figure 5) acquired at 263 K, 11.7 T, 12.5 kHz MAS, and with ^{13}C{^{1}H} contact time of (A) 0.5 ms and (B) 5 ms. All of the ^{13}C signals are assigned to ^{13}C moieties on the TMAda$^+$ and D6$_{1,2}$ molecules as indicated on the molecular structures in the inset. 1D ^{13}C{^{1}H} CP-MAS or ^{1}H spin-echo spectra acquired under the same conditions as the 2D spectra are shown along the corresponding ^{13}C or ^{1}H axes for comparison with the 1D projections of the 2D spectra. Correlated ^{13}C{^{1}H} signal intensities that arise from the TMAda$^+$ molecules, D6$_{1,2}$ tail moieties, or D6$_{1,2}$ headgroup moieties are indicated with red, green, and blue boxes, respectively, while correlated signals arising from intermolecular interactions among the different OSDA molecules are indicated by purple boxes. The presence of correlated signals from intermolecular interactions establishes the mutual nanoscale proximities (<1 nm) of the D6$_{1,2}$ and TMAda$^+$ molecules.
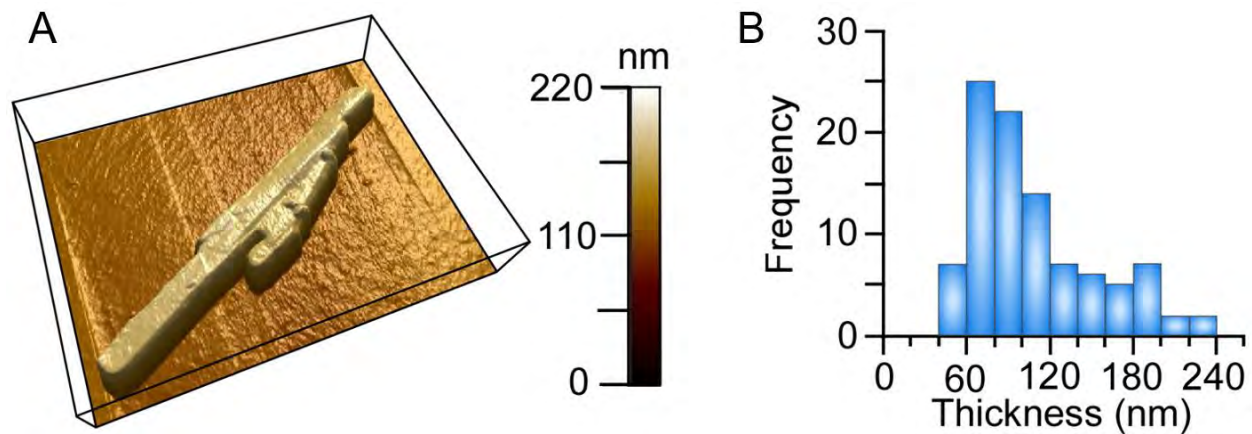
Figure S11. (A) 3-dimensional AFM height mode image of a HOU-4 crystal that was extracted from a growth solution (after washing with DI water) and dried on a silicon wafer. (B) Particle size distribution of HOU-4 crystals from multiple AFM samples prepared from a single zeolite synthesis batch. The thickness measured along the [100] direction of ultrathin mordenite crystals was measured *ex situ* (in air) by AFM.
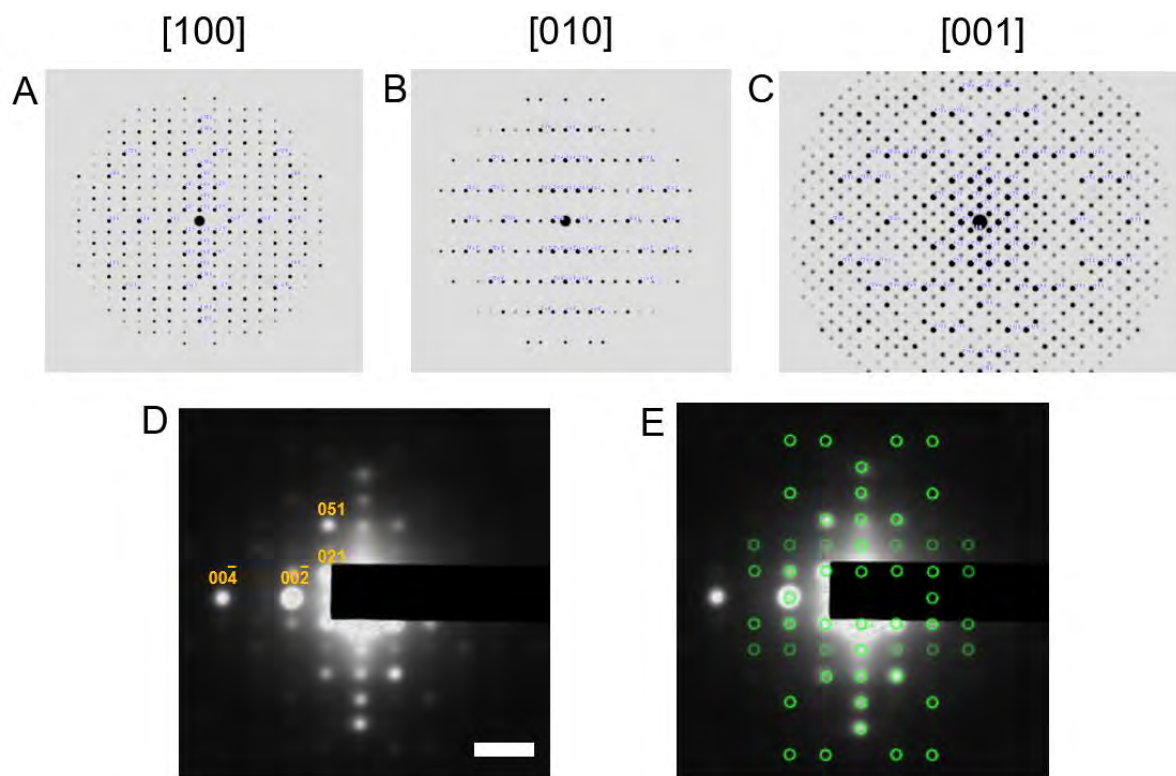
Figure S12. Simulated electron diffraction patterns along three zone axes of mordenite: (A) [100], (B) [010], and (C) [001]. (D) The SAED pattern in Figure 2E with labelled indices of the [100] zone axis. (E) The same SAED pattern with a mask of the [100] zone axis from predicted pattern in (A) that is overlaid on the measured pattern. Excellent agreement between the measured and predicted patterns are consistent with HRTEM data (Figure 2).
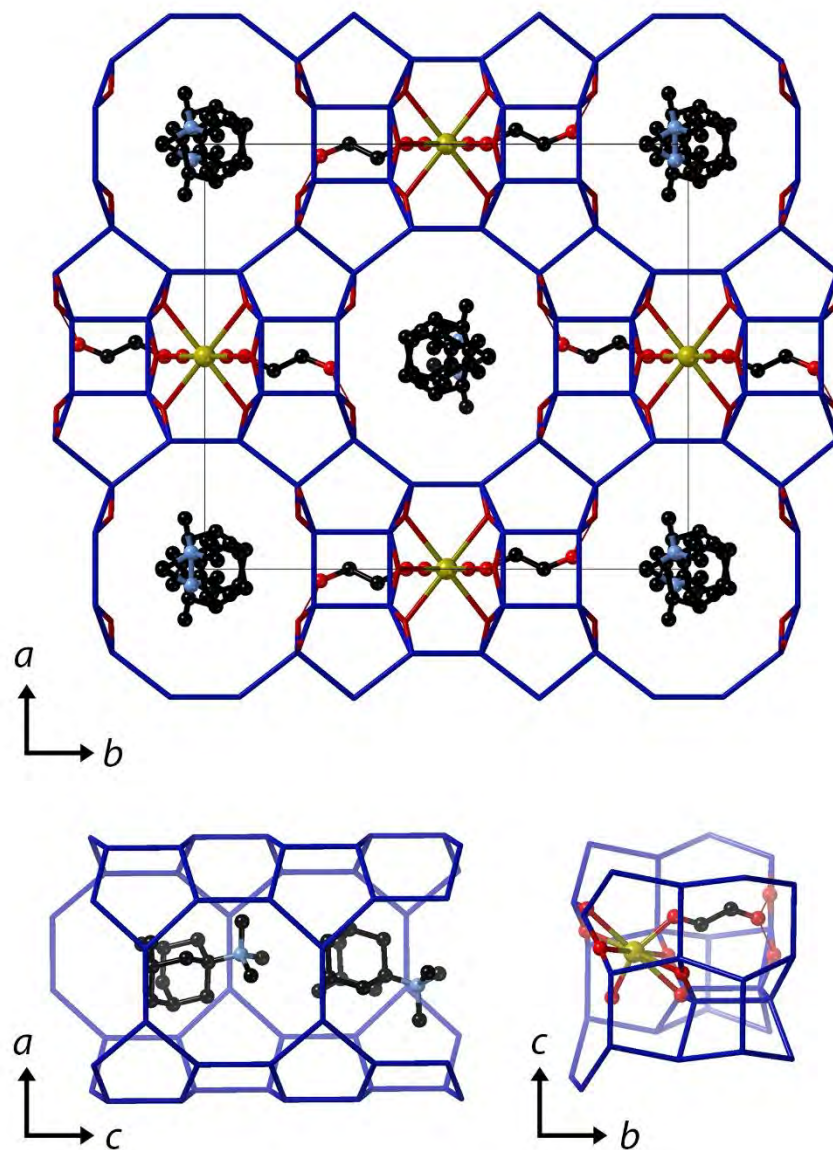
Figure S13. The refined structure of HOU-4 showing (A) a possible arrangement of the non-framework species in the channels and cavities, (B) the TMAda$^+$/DMAda species in the 12-ring channel, and (C) the Na$^+$ ion in the oval 8-ring channel coordinated to 6 framework O atoms, one water molecule, and an O atom of D6$_{1,2}$. The second O atom of D6$_{1,2}$ is within hydrogen bonding distance of two framework O atoms. For clarity, only the framework O atoms interacting with the non-framework species are shown.
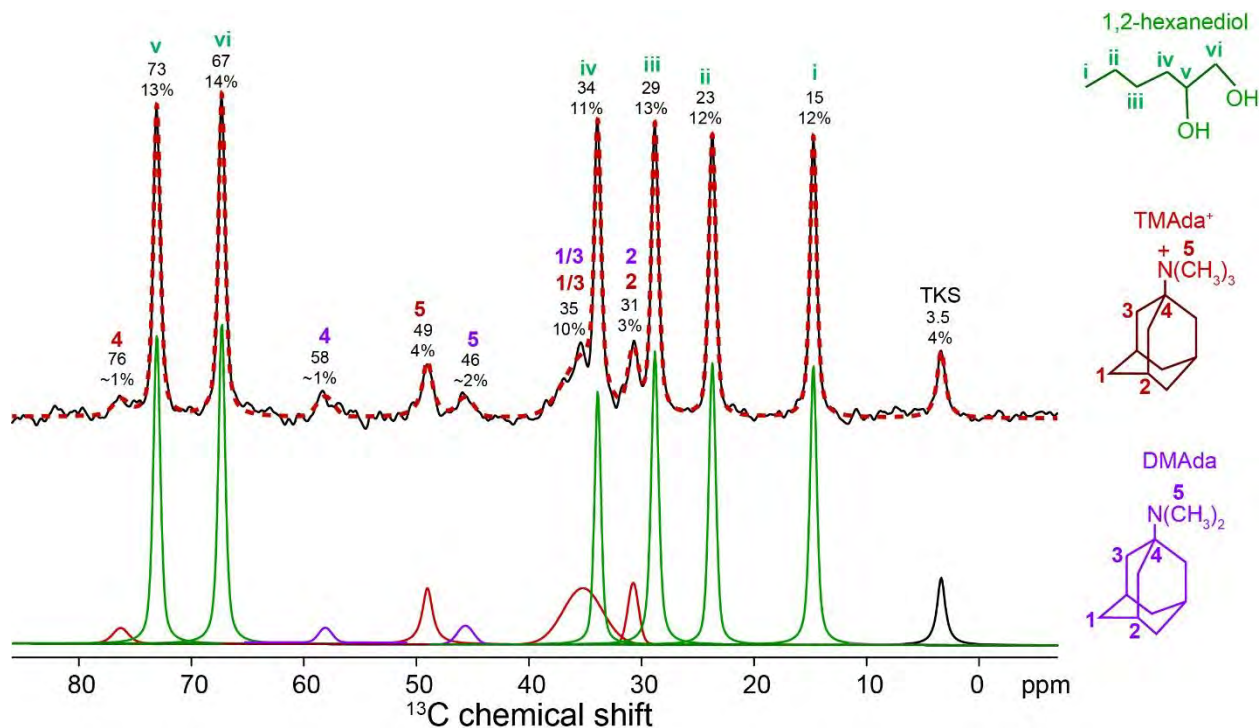
Figure S14. Solid-state quantitative single-pulse 1D ^{13}C NMR spectrum of as-made HOU-4 (same sample as Figures 5 and S10), acquired at 11.7 T, 298 K, and 12.5 kHz MAS. The fit deconvolution is offset below the 1D spectrum. The signal at 3.5 ppm arises from TKS, which was added as an internal spin counting reference to determine the absolute quantities of occluded OSDA molecules in HOU-4. Analyses of the relative integrated intensities of the different ^{13}C NMR signals establish an organic content of 1.2-1.3 μmol hexanediol, 0.1-0.2 μmol TMAda$^+$, and 0.05-0.1 μmol DMAda per mg HOU-4. Thus, there is approximately an order of magnitude more D6$_{1,2}$ species than TMAda$^+$.
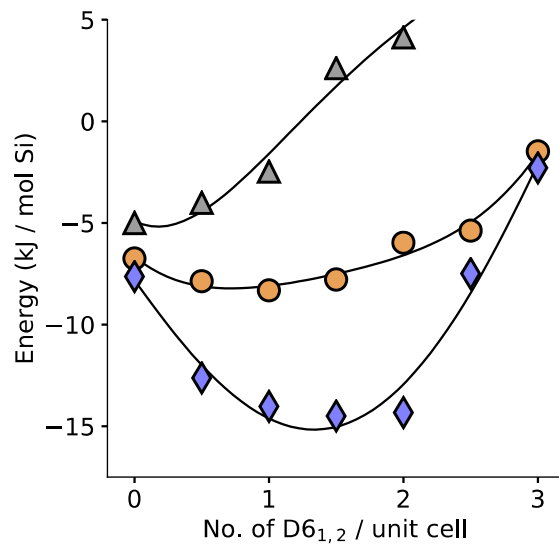
Figure S15. MD calculation of the stabilization energy for organics occluded in mordenite as a function of $D6_{1,2}$ loading at fixed $TMAda^+$ loadings of 1.0 (orange), 1.5 (blue), and 2.0 (grey) per unit cell. Solid lines are guides for the eye.
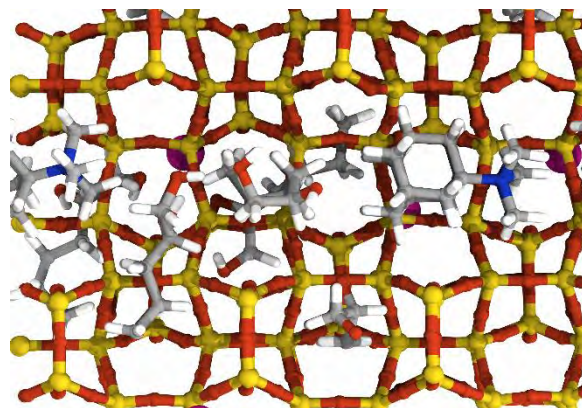
Figure S16. Rendering of a configuration from an MD simulation showing $D6_{1,2}$ in the 12-ring channel of mordenite between adjacent TMAda$^+$ molecules (c-direction oriented to the right). The loadings for $D6_{1,2}$ and TMAda$^+$ are both 1.5 per unit cell. Atoms are color coded as grey (carbon), red (oxygen), blue (nitrogen), white (hydrogen), and yellow (T-sites occupied by silicon or aluminum).
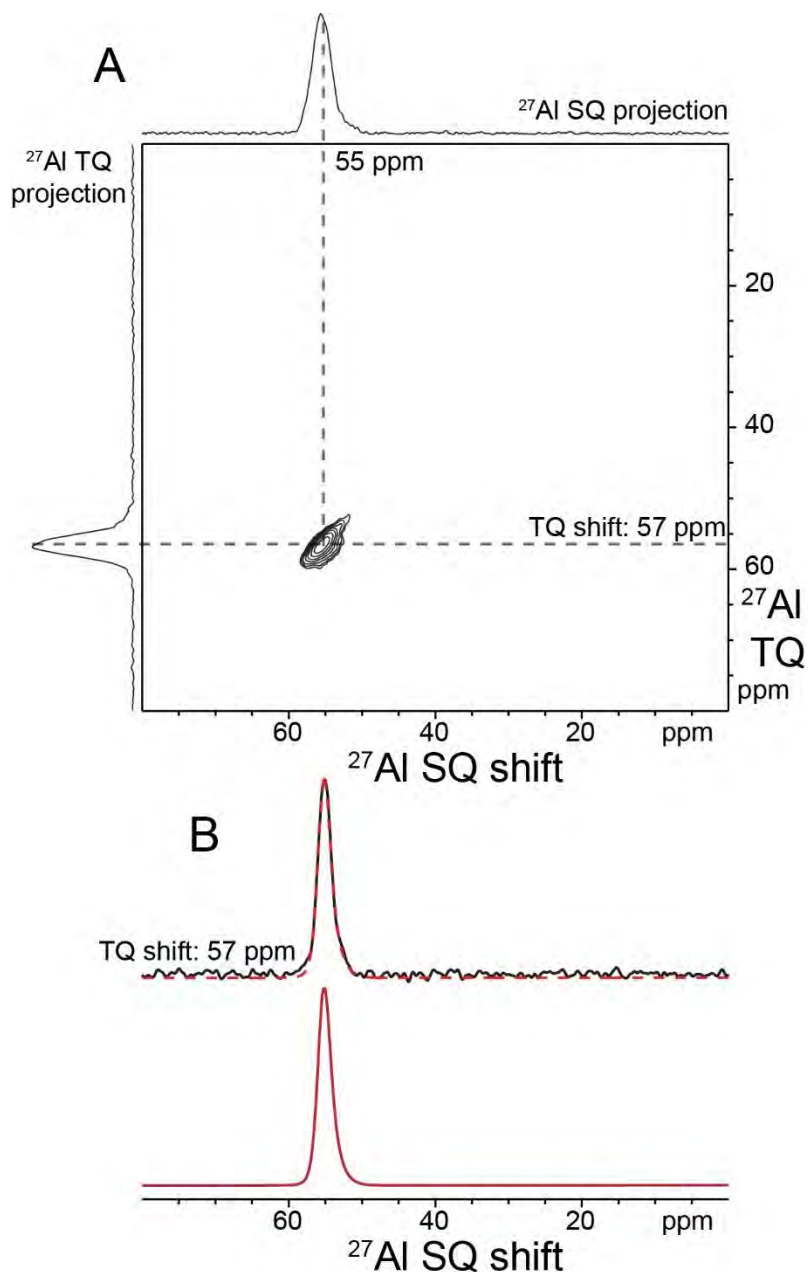
Figure S17. (A) 2D ^{27}Al triple-quantum MAS (3QMAS) NMR spectrum of as-made HOU-4 (same sample as Figures 5, S10, and S14) acquired at 18.8 T, 298 K, and 20 kHz MAS. The inhomogeneously-broadened ^{27}Al spectrum exhibits a Czjzek lineshape, as corroborated in (B) by comparing a single-quantum (SQ) slice of the 2D 3QMAS spectrum extracted at a triple-quantum (TQ) shift of 57 ppm (black) to a simulated ^{27}Al Czjzek lineshape (dotted red). The simulated ^{27}Al spectrum is shown offset below in red. The fitted Czjzek parameters were a 1.4 ppm chemical shift FWHM and a maximum nuclear quadrupolar coupling constant (C_Q) value of 1600 kHz. The simulation was performed using dmfit software.[15]
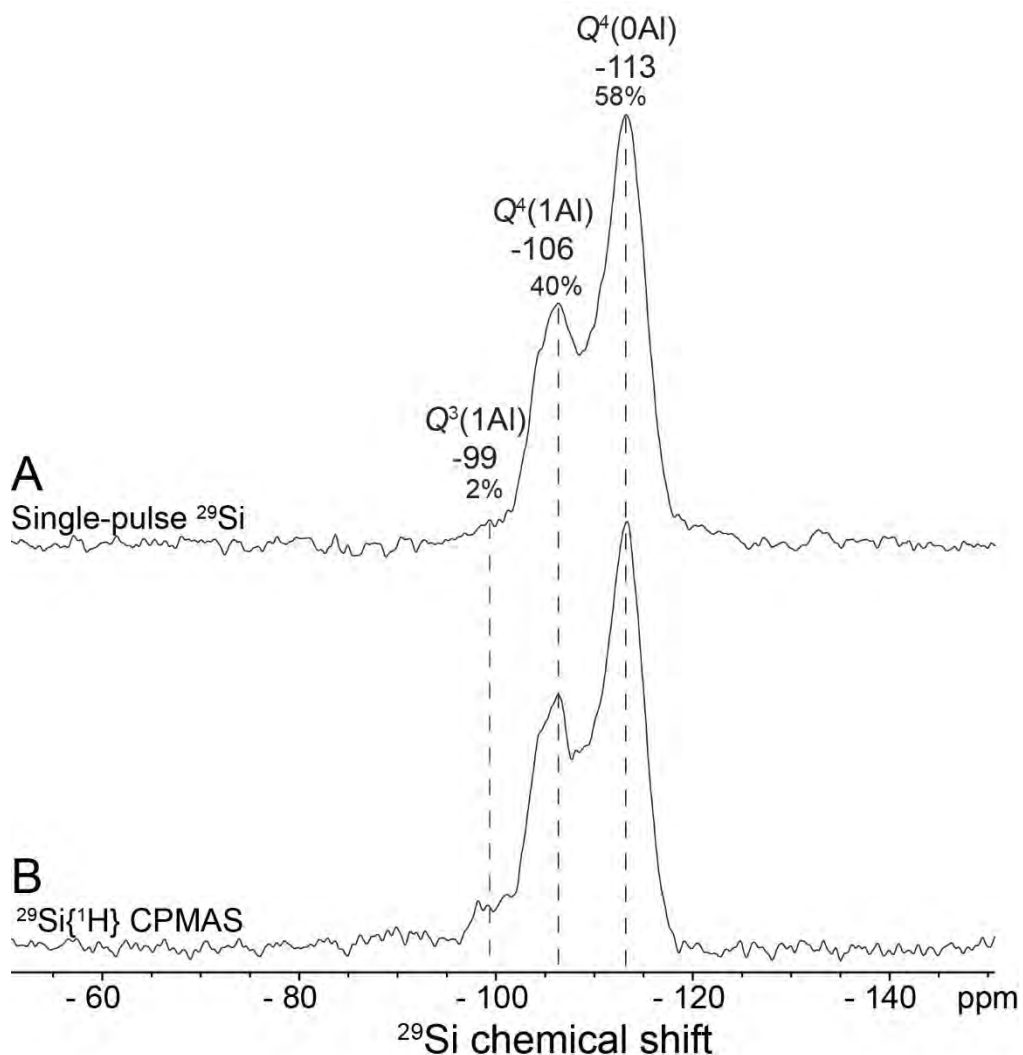
Figure S18. 1D ^{29}Si NMR spectra of calcined HOU-4 acquired at 11.7 T and 298 K: (A) quantitative single-pulse ^{29}Si NMR spectrum, acquired at 10 kHz MAS and with a recycle delay of 120 s for full spin-lattice relaxation of the ^{29}Si nuclei within the zeolite, and (B) ^{29}Si{^{1}H} CP MAS NMR spectrum, acquired with a contact time of 5 ms, a recycle delay of 1 s, and at 5 kHz MAS. The ^{29}Si signal at -99 ppm arises from dilute partially-crosslinked Q^3(1Al) moieties that are likely associated with defect sites at the HOU-4 crystal surfaces.
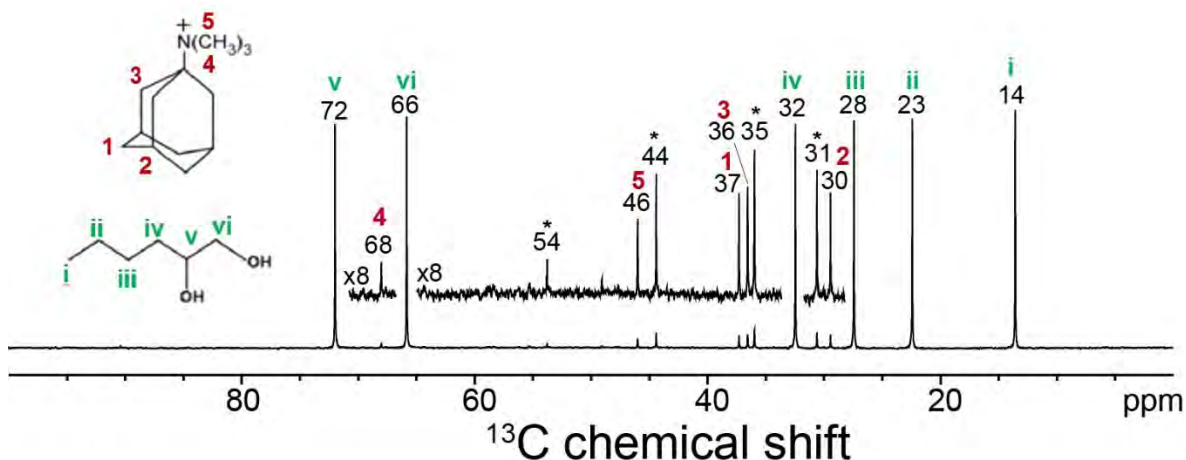
Figure S19. Solution state 1D ^{13}C NMR spectrum of the HOU-4 synthesis supernatant solution, diluted with 10% D$_2$O by volume. The ^{13}C signals assigned to ^{13}C moieties on the TMAda$^+$ and D6$_{1,2}$ molecules are labeled with red numbers and green Roman numerals, respectively, as indicated on the molecular structures in the inset. Signals assigned to decomposition products of TMAda$^+$ are indicated with asterisks. Based on their ^{13}C shifts, all of the ^{13}C signals from TMAda$^+$ decomposition products are assigned to dimethyladamantamine, DMAda.[11] From the relative integrated intensities of the ^{13}C NMR signals, the supernatant solution contains TMAda$^+$, adamantanol, and D6$_{1,2}$ at approximate molar ratios of 1 TMAda$^+$: 2 DMAda : 50 D6$_{1,2}$.
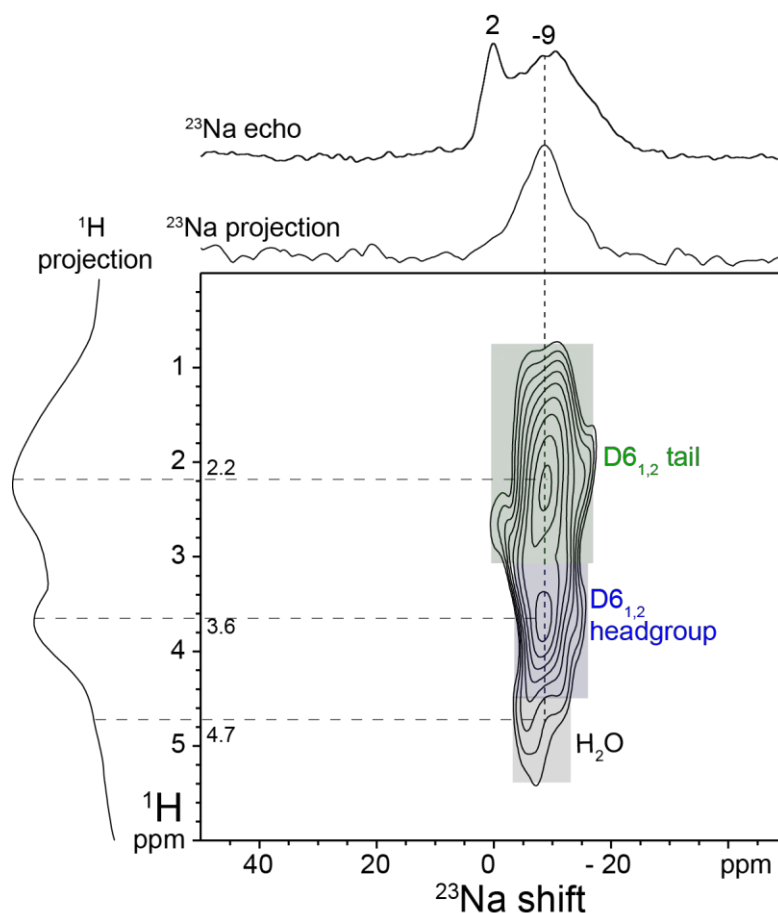
Figure S20. Solid-state 2D ^{23}Na{^{1}H} NMR correlation spectrum of HOU-4 (same sample as Figures 5, S10, S14, and S17) acquired at 263 K, 18.8 T, 12.5 kHz MAS, and with a ^{23}Na{^{1}H} contact time of 0.2 ms. A 1D ^{23}Na echo spectrum acquired under the same conditions is shown along the horizontal axis for comparison with the 1D ^{23}Na projection of the 2D spectrum. Correlated ^{23}Na{^{1}H} signal intensities that arise from interactions with the D6$_{1,2}$ tail and headgroup moieties are indicated with green and blue boxes, respectively. The 1D ^{23}Na echo MAS spectrum shows ^{23}Na signals at 2 and -9 ppm, assigned to Na$^+$ species in different local environments.[16] Only the ^{23}Na signal at -9 ppm is enhanced in the 2D ^{23}Na{^{1}H} HETCOR spectrum, indicating that the ^{23}Na signal at 2 ppm is likely associated with an anhydrous impurity phase. The ^{23}Na signal at -9 ppm is correlated with ^{1}H signals at 2.2 and 3.6 ppm, assigned respectively to D6$_{1,2}$ tail and headgroup moieties. These correlated signals are consistent with the association of Na$^+$ cations in the 8-ring side pockets to D6$_{1,2}$ molecules. A shoulder at 4.7 ppm in the ^{1}H dimension (gray box) likely arises from H$_2$O molecules coordinated the Na$^+$ species. Overall, the ^{23}Na spectra are consistent with the siting of Na$^+$ cations in HOU-4 exclusively in the 8-ring side pockets, where they coordinate to D6$_{1,2}$ and water molecules.
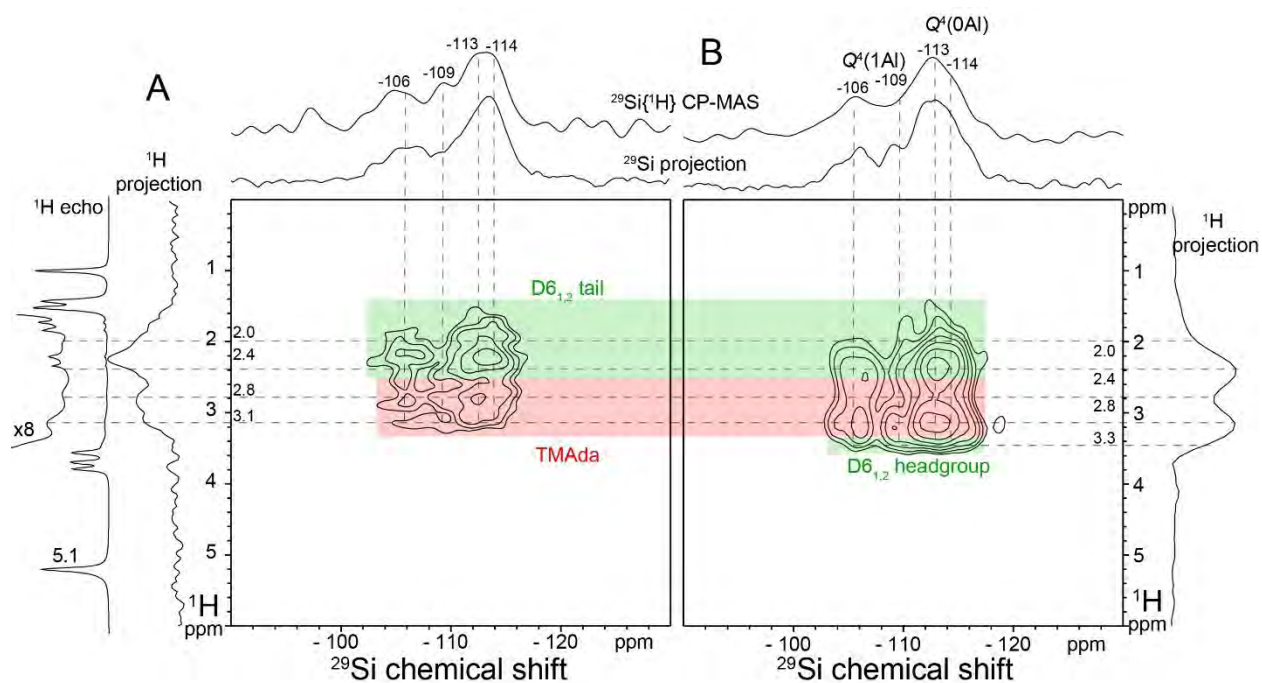
Figure S21. Solid-state 2D ^{29}Si{^{1}H} NMR correlation spectra of HOU-4 (same sample as Figures 5, S10, S14, S17, and S20) acquired at 263 K, 11.7 T, 12.5 kHz MAS, and with ^{29}Si{^{1}H} contact times of (A) 0.2 ms and (B) 5 ms. 1D ^{29}Si{^{1}H} CP-MAS and ^{1}H spin-echo spectra acquired under the same conditions as the 2D spectra are shown along the horizontal and vertical axes, respectively, for comparison with the 1D ^{29}Si and ^{1}H projections of the 2D spectrum. Correlated ^{29}Si{^{1}H} signal intensities that arise from interactions with the TMAda$^+$ and D6$_{1,2}$ molecules are indicated with red and green boxes, respectively. All of the ^{29}Si signals are correlated with all of the ^{1}H signals from the different OSDA moieties, consistent with the mutual proximities (<1 nm) of the OSDA molecules within the nanopores of HOU-4.
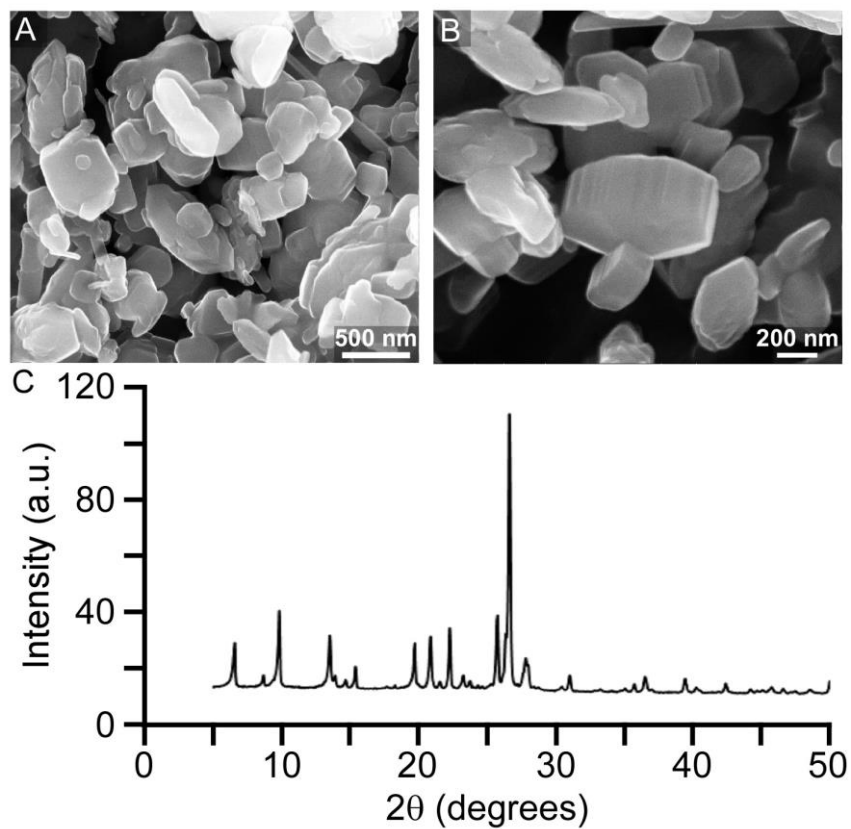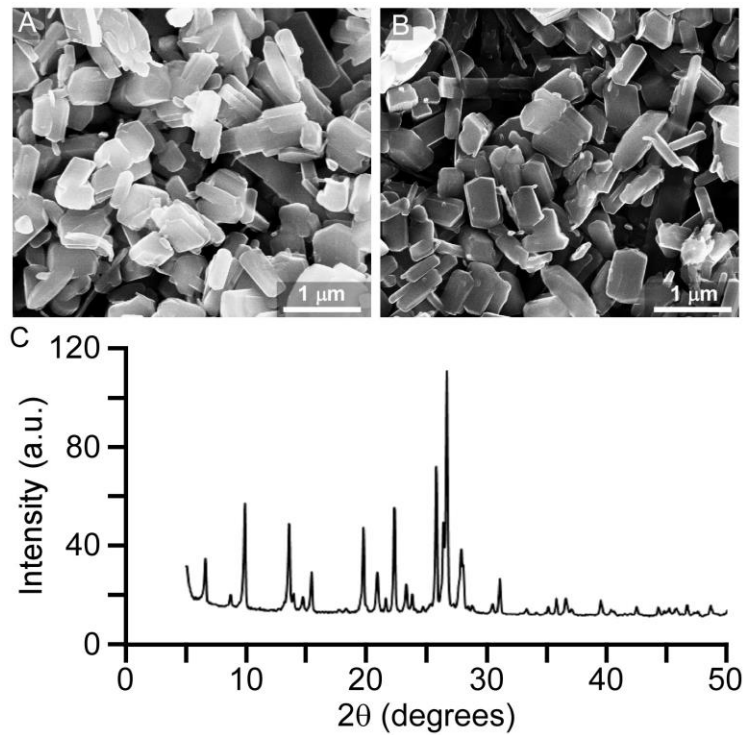
Figure S22. (A and B) Scanning electron micrographs of a modified HOU-4 synthesis using composition C1 (Table S1) with an alteration in the quantity of OSDA (i.e., using a molar ratio of 3.0 $D6_{1,2}$:1.0 SiO_2). (C) Corresponding XPD pattern of as-made mordenite product.

Figure S23. (A and B) Scanning electron micrographs of a modified HOU-4 synthesis using composition C1 (Table S1) with an alteration in the quantity of silica (i.e., using a molar ratio of 0.9 SiO_2: 1.44 $D6_{1,2}$). (C) Corresponding XPD pattern of as-made mordenite (**MOR**) product.
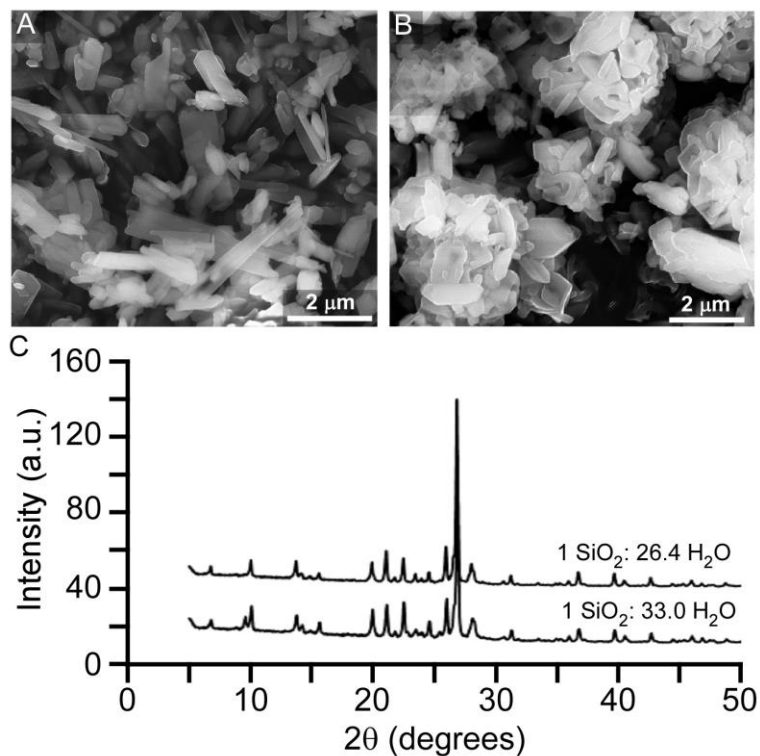
Figure S24. Scanning electron micrographs of a modified HOU-4 synthesis using composition C1 (Table S1) with an alteration in the quantity of water: (A) 25% reduction using a molar ratio of 33 H_2O:1.0 SiO_2; (B) 40% reduction using a molar ratio of 26.4 H_2O:1.0 SiO_2. (C) Corresponding XPD pattern of as-made mordenite products at lower water content.
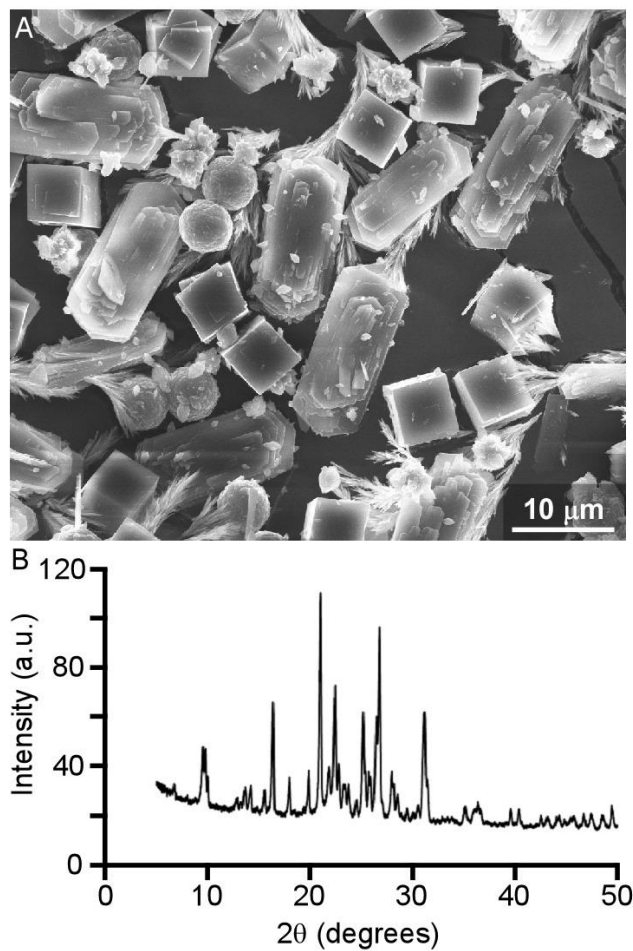
Figure S25. (A) Scanning electron micrograph of solids extracted from a synthesis with molar composition C2 modified with the diol D4$_{1,2}$ (Table S1). (B) Corresponding XPD pattern of the mordenite product which shows two impurities: SSZ-13 and quartz.
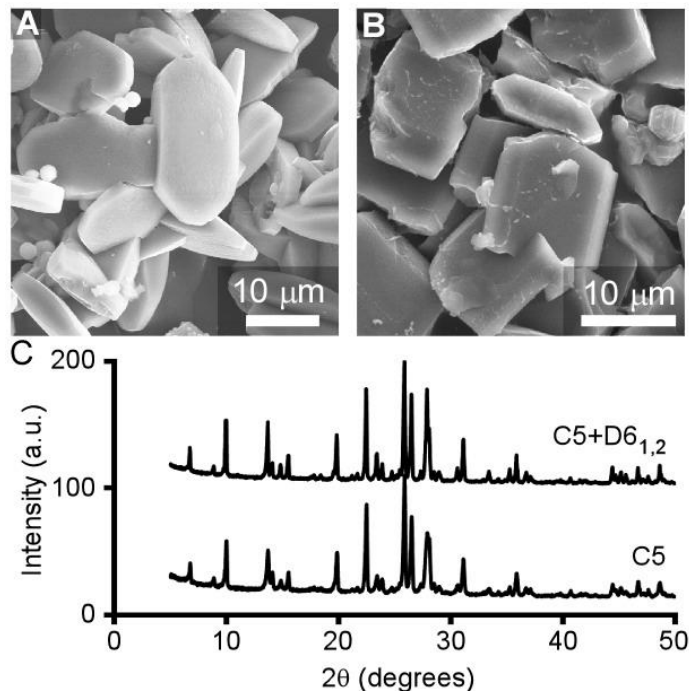
Figure S26. (A) Scanning electron micrograph of conventional mordenite crystals obtained using composition C5 with a molar ratio of 6 Na_2O: 1 Al_2O_3: 30 SiO_2: 780 H_2O. (B) SEM image of mordenite crystals obtained using composition C5 with 1.6 $D6_{1,2}$:1.0 SiO_2. (C) XPD pattern for conventional mordenite synthesis (bottom) compared to the same synthesis with the addition of $D6_{1,2}$ (top).
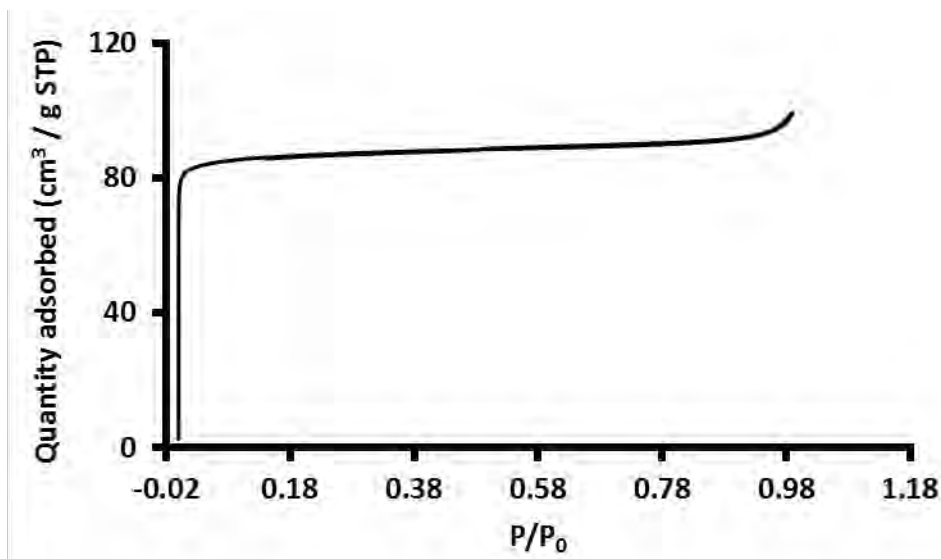

Figure S27. Nitrogen adsorption/desorption isotherm for HOU-4 (prepared with growth solution C1) with a corresponding BET surface area of 339 m^2/g that reflects a mixture of mordenite and quartz impurity in the sample. The BET surface area for conventional mordenite (prepared with growth solution C5) is reported by Pastvova et al. to be 240 m^2/g.[17]

Movie S1. A 2-ns molecular dynamics (MD) trajectory illustrating the mobility of $D6_{1,2}$ in the main channel of mordenite. The main channel is rendered as a semitransparent cylinder, and only a cross section of the zeolite framework is shown for clarity.

References

1. Hanwell, M.D., D.E. Curtis, D.C. Lonie, T. Vandermeersch, E. Zurek, and G.R. Hutchison, *Avogadro: an advanced semantic chemical editor, visualization, and analysis platform.* Journal of Cheminformatics, 2012. **4**.

2. Kihara, K., *An X-ray Study of the Temperature-dependence of the Quartz Structure.* European Journal of Mineralogy, 1990. **2**: 63-77.

3. Meier, W.M., *The crystal structure of mordenite (ptilolite).* Zeitschrift für Kristallographie, 1961. **115**: 439-450.

4. Smeets, S., L.B. McCusker, C. Baerlocher, S. Elomari, D. Xie, and S.I. Zones, *Locating Organic Guests in Inorganic Host Materials from X-ray Powder Diffraction Data.* Journal of the American Chemical Society, 2016. **138**: 7099-7106.

5. Lu, B.W., Y. Oumi, and T. Sano, *Convenient synthesis of large mordenite crystals.* Journal of Crystal Growth, 2006. **291**: 521-526.

6. Oumi, Y., Y. Kakinaga, T. Kodaira, T. Teranishi, and T. Sano, *Influences of aliphatic alcohols on crystallization of large mordenite crystals and their sorption properties.* Journal of Materials Chemistry, 2003. **13**: 181-185.

7. Berkson, Z.J., R.J. Messinger, K. Na, Y. Seo, R. Ryoo, and B.F. Chmelka, *Non-Topotactic Transformation of Silicate Nanolayers into Mesostructured MFI Zeolite Frameworks During Crystallization.* Angewandte Chemie-International Edition, 2017. **56**: 5164-5169.

8. Smeets, S., Z.J. Berkson, D. Xie, S.I. Zones, W. Wan, X.D. Zou, M.F. Hsieh, B.F. Chmelka, L.B. McCusker, and C. Baerlocher, *Well-Defined Silanols in the Structure of the Calcined High-Silica Zeolite SSZ-70: New Understanding of a Successful Catalytic Material.* Journal of the American Chemical Society, 2017. **139**: 16803-16812.

9. d'Espinose de la Caillerie, J.B., C. Fretigny, and D. Massiot, *MAS NMR spectra of quadrupolar nuclei in disordered solids: The Czjzek model.* Journal of Magnetic Resonance, 2008. **192**: 244-251.

10. Anderson, M.W., P.J. Barrie, and J. Klinowski, *H-1 Magic-Angle-Spinning NMR-Studies of the Adsorption of Alcohols on Molecular-Sieve Catalysts.* Journal of Physical Chemistry, 1991. **95**: 235-239.

11. Pehk, T., E. Lippmaa, Sevostja.Vv, A.I. Tarasova, and Krayusch.Mm, *C-13 NMR-Spectra of Adamantane Derivatives.* Omr-Organic Magnetic Resonance, 1971. **3**: 783-&.

12. Adams, B.L. and P. Kovacic, *Hofmann Elimination and Stevens Rearrangement with N,N,N-trimethyl-3-homoadamantylammonium Hydroxide - Evidence for 3-Homoadamantene.* Journal of Organic Chemistry, 1974. **39**: 3090-3094.

13. *CrystalMaker Software.* http://crystalmaker.com/singlecrystal/.

14. Baerlocher, C. and L.B. McCusker, *Database of Zeolite Structures.* http://www.iza-structure.org/databases/.

15. Massiot, D., F. Fayon, M. Capron, I. King, S. Le Calve, B. Alonso, J.O. Durand, B. Bujoli, Z.H. Gan, and G. Hoatson, *Modelling one- and two-dimensional solid-state NMR spectra.* Magnetic Resonance in Chemistry, 2002. **40**: 70-76.

16. Koller, H., G. Engelhardt, A.P.M. Kentgens, and J. Sauer, *^{23}Na NMR Spectroscopy of Solids: Interpretation of Quadrupole Interaction Parameters and Chemical Shifts.* Journal of Physical Chemistry, 1994. **98**: 1544-1551.

17. Pastvova, J., D. Kaucky, J. Moravkova, J. Rathousky, S. Sklenak, M. Vorokhta, L. Brabec, R. Pilar, I. Jakubec, E. Tabor, P. Klein, and P. Sazama, *Effect of Enhanced Accessibility of Acid Sites in Micromesoporous Mordenite Zeolites on Hydroisomerization of n-Hexane.* Acs Catalysis, 2017. **7**: 5781-5795.